Palaeogeography, Palaeoclimatology, Palaeoecology 553 (2020) 109799

Contents lists available at ScienceDirect

Palaeogeography, Palaeoclimatology, Palaeoecology

journal homepage: www.elsevier.com/locate/palaeo

Integrated sedimentary, biotic, and paleoredox dynamics from multiple localities in southern Laurentia during the late Silurian (Ludfordian) extinction event

Chelsie N. Bowman[a,*], Anders Lindskog[a,b], Nevin P. Kozik[a], Claudia G. Richbourg[a], Jeremy D. Owens[a], Seth A. Young[a]

[a] Department of Earth, Ocean, & Atmospheric Sciences | National High Magnetic Field Laboratory, Florida State University, Tallahassee, Florida 32306, USA
[b] Department of Geology, Lund University, Sölvegatan 12, SE-223 62 Lund, Sweden

ARTICLE INFO

Keywords:
Sulfur isotopes
Iodine
Microfacies
Anoxia
Euxinia
Sea level

ABSTRACT

The Silurian was a time of major climatic transition punctuated by multiple biotic crises and global carbon cycle perturbations. The most severe of these biotic events was the late Silurian (Ludfordian) Lau/Kozlowskii extinction event (LKE) and the associated Lau carbon isotope excursion (CIE). Although the extinction event and Lau CIE are globally documented, the only records thus far of local and global marine paleoredox conditions through this interval are from a single region in Scandinavia. Here we examine four sections along a bathymetric transect of mixed carbonate-siliciclastic sediments from western Tennessee, USA. A novel approach using a multi-proxy dataset combining high-resolution geochemical data and microfacies analyses from multiple localities explores the possibilities of local/regional-scale redox heterogeneities during a time of widespread environmental upheaval on a global scale. Paired positive excursions recorded in carbonate carbon isotopes and carbonate-associated sulfate sulfur isotopes support recent work from carbonate and siliciclastic successions from Scandinavia, suggesting a global enhancement of organic carbon and pyrite burial driven by an expansion of euxinic (anoxic and sulfidic water column) conditions in the oceans during the mid-Ludfordian. Furthermore, positive excursions in organic carbon isotopes and pyrite sulfur isotopes reflect the global changes in redox. Stratigraphic trends in I/Ca ratios imply a local expansion of low-oxygen conditions, with low, but non-zero values during the rising limb and peak of the CIE. The fossil assemblages vary across the shelf and through the CIE interval. Stratigraphic changes in fossil assemblages and I/Ca are closely associated with local and global changes in oxygenation and sea level during the mid-Ludfordian. The collective data indicate significant biotic reorganization in response to changes in marine redox conditions and in conjunction with sea-level variation during the LKE interval, but detailed macroscopic biodiversity is currently unconstrained for this region.

1. Introduction

The Silurian Period was a climatically dynamic time in the middle Paleozoic marked by repeated extinctions, faunal reorganizations, and carbon cycle perturbations. In less than 30 million years there were at least four globally documented positive carbon isotope excursions (CIE) greater than +4‰, indicating higher magnitude carbon-cycle volatility than any other period in the Phanerozoic (Bickert et al., 1997; Kaljo et al., 1997; Saltzman, 2001, 2002; Cramer and Saltzman, 2007; Saltzman and Thomas, 2012). The largest magnitude perturbation to the Silurian global carbon cycle was the mid-Ludfordian Lau CIE, with peak excursion values averaging +5 to +8‰ and as high as +12‰; it is also considered the largest positive carbon isotope excursion in the Phanerozoic (Munnecke et al., 2003; see Calner, 2008 for review). The Lau CIE is associated with the Lau/Kozlowskii extinction (LKE) event, which is at least the tenth most severe extinction in Earth history with a loss of ~23% of marine genera (Bond and Grasby, 2017 and references therein). This extinction was first recognized in conodonts from carbonate platform successions as the 'Lau event' (Jeppsson, 1990) and in studies of graptolites in deeper-water shales as the 'Kozlowskii event' (Koren, 1993; Urbanek, 1993). As extinctions have been recognized in an increasing variety of marine fauna, a curiously asynchronous pattern of extinction has become apparent (e.g., Munnecke et al., 2003; Stricanne et al., 2006; compiled in Bowman et al., 2019). Extinctions in

* Corresponding author.
E-mail addresses: cnb09@my.fsu.edu (C.N. Bowman), anders.lindskog@geol.lu.se (A. Lindskog), npk15@my.fsu.edu (N.P. Kozik), crichbou@uwyo.edu (C.G. Richbourg), jdowens@fsu.edu (J.D. Owens), sayoung2@fsu.edu (S.A. Young).

https://doi.org/10.1016/j.palaeo.2020.109799
Received 17 January 2020; Received in revised form 10 May 2020; Accepted 11 May 2020
Available online 14 May 2020

benthic and nektonic taxa such as conodonts, fish (Eriksson et al., 2009), and brachiopods (Talent et al., 1993) notably precede those of planktic taxa such as graptolites and acritarchs (Stricanne et al., 2006). Widespread development of 'anachronistic' (both microbially-mediated and abiotic) carbonate facies has also been linked to the LKE as evidence of environmental stress and ecosystem collapse (e.g., Calner, 2005). Much of the work on the record of biotic change during the LKE has been done on the paleocontinents of Baltica (Latvia, Sweden; e.g., Jeppsson, 1990; Stricanne et al., 2006; Eriksson et al., 2009; Urbanek et al., 2012) and Gondwana (Australia, Czech Republic; e.g., Jeppsson et al., 2007; Lehnert et al., 2007; Manda et al., 2012). Comparatively little is known about the Laurentian expression of this extinction event.

High-magnitude positive CIEs can result from increased weathering of carbonate platforms during sea-level lowstand (e.g., Berner, 1994; Kump et al., 1999) and/or from enhanced organic carbon burial via productivity- or preservation-driven expansion of anoxia (Arthur et al., 1988; Kump and Arthur, 1999; Cramer and Saltzman, 2005, 2007; Gill et al., 2011a; Owens et al., 2018). A gradual expansion of reducing conditions has been proposed as a kill mechanism for the LKE, which can account for the asynchronous nature of the extinction event and also the global CIE (e.g., Munnecke et al., 2003; Stricanne et al., 2006). A recent study using thallium isotopes from the Baltic Basin has shown that global marine deoxygenation predates the Lau CIE and is coeval with the onset of the LKE (Bowman et al., 2019). Additionally, parallel positive carbon and sulfur isotope excursions are documented following the initial global deoxygenation, indicating that enhanced organic carbon burial was closely associated with the expansion of euxinic conditions (anoxic with water-column sulfide) in the late Silurian oceans (Bowman et al., 2019).

During global scale biogeochemical events, such as the Lau CIE, only an increase in the fraction of ocean floor experiencing reducing conditions is proposed (i.e., not anoxia or euxinia throughout the entire ocean). Many previous studies have used geochemical box modeling to estimate the extent of marine anoxia and/or euxinia during similar events, determining that increases in the extent of anoxia/euxinia to only ~5–10% of the global seafloor are necessary to drive these geochemical perturbations (e.g., Gill et al., 2011a; Owens et al., 2013; Reinhard et al., 2013; Dickson et al., 2016; Lau et al., 2016; Zhang et al., 2018; Young et al., 2019). The temporal evolution of local redox conditions, however, has not been extensively studied for a bathymetric transect across the Lau CIE to understand local heterogeneities compared to the globally integrated signal. Here we present an innovative combination of high-resolution geochemical and microfacies data from four sections across a transect of the mixed carbonate and siliciclastics deposited on the Western Tennessee Shelf (Tennessee, USA), to better constrain both spatiotemporal redox changes and heterogeneities through the LKE and Lau CIE interval across this shelf setting. To understand if and how paleoredox changes varied with changes in the global carbon cycle, we measured paired carbon ($\delta^{13}C_{carb}$ and $\delta^{13}C_{org}$) and sulfur ($\delta^{34}S_{CAS}$ and $\delta^{34}S_{pyr}$) isotopes and I/Ca ratios (representative of I/(Ca + Mg) values). To assess faunal and other paleoenvironmental changes, such as changes in sea level, detailed field studies were combined with petrographic analyses of carbonate composition, fabrics, and textures at the microscopic scale (i.e., microfacies). The combination of these datasets provides a holistic view of the biotic and geochemical evolution of this late Silurian carbonate shelf.

2. Background

2.1. Geologic setting and conodont biostratigraphy

The four study sites were located along the southern margin of the paleocontinent Laurentia during the late Silurian (Fig. 1A, B) along a gently sloping, sub-tropical to tropical, mixed carbonate and siliciclastic ramp known as the Western Tennessee Shelf (Broadhead and Gibson, 1996; Barrick et al., 2010). Paleogeographic reconstructions of the Silurian place the southern margin of Laurentia between 20 and 30°S (Cocks and Scotese, 1991; Cocks and Torsvik, 2002; Torsvik and Cocks, 2017). The Western Tennessee Shelf area was bounded by the Nashville Dome to the east, the Reelfoot Rift Embayment to the west/northwest, and the continental margin to the south (present-day directions; Fig. 1B). The upper Silurian rocks exposed in the study area form a transect from shallower- to deeper-ramp settings approximately from the southeast to northwest, towards the Reelfoot Rift Embayment (Barrick et al., 2010).

The upper Silurian (Ludfordian) Brownsport Formation is exposed in multiple roadcuts in the area northwest of Waynesboro, TN, along highways US-64, US-641, and TN-228 near the Tennessee River. The Brownsport Formation conformably overlies the Dixon Formation, which is comprised largely of red and green mottled calcareous mudstones (Amsden, 1949; Broadhead and Gibson, 1996). It is conformably overlain by the Decatur Limestone, a typically light grey, massively bedded crystalline limestone (Amsden, 1949). The Brownsport Formation itself is subdivided into three members, in ascending stratigraphic order: Beech River, Bob, and Lobelville (Pate and Bassler, 1908; Broadhead and Gibson, 1996; Barrick et al., 2010). The Beech River and Lobelville members are lithologically similar, being composed primarily of argillaceous wackestones and packstones that are commonly interbedded with calcareous shales; coarser-grained, locally sandy, packstones and grainstones make up the Bob Member (Pate and Bassler, 1908; Amsden, 1949; Broadhead and Gibson, 1996; Barrick et al., 2010). There has been detailed discussion on the decision to break up the Brownsport into finer-scale, formal lithologic units (e.g., Pate and Bassler, 1908; Amsden, 1949; Broadhead and Gibson, 1996; Barrick et al., 2010), largely because the Bob Member is not readily identifiable in all exposures of the Brownsport Formation and the Beech River and Lobelville members are lithologically similar (Amsden, 1949). Some studies have tried to break up the Brownsport Formation based on macrofaunal assemblages (e.g., Pate and Bassler, 1908), but these subdivisions appear to be inconsistent between sections (see also results herein, Section 4.1; Supplemental Materials).

Conodont biostratigraphy and carbon isotope chemostratigraphy have previously been investigated in this region (Barrick et al., 2010) at the Eagle Creek and Linden sections, the four sections in this study are near these two previously described sections. Barrick et al. (2010) reported the presence of the *Polygnathoides siluricus* Zone in the Beech River Member and the beginning of the *Ozarkodina snajdri* Zone near the base of the Bob Member. Barrick et al. (2010) found no record in the Brownsport Formation of the impoverished fauna of the Icriodontid Zone that is recognized on Gotland, Sweden (the 'type area' of the Lau interval; e.g., Jeppsson, 2005), between the *P. siluricus* and *O. snajdri* zones. The upper Bob and the Lobelville members yield very few conodont elements and thus the *Ozarkodina crispa* Zone has not been confidently identified in the Brownsport Formation; for reference, we use the latest Silurian global conodont biozonation scheme of McAdams et al. (2019). Chemostratigraphic correlation with the Gotland record (e.g., Bowman et al., 2019) of the Lau CIE suggests that the *O. crispa* Zone would begin in the falling limb of the CIE, corresponding to a level close to the Bob–Lobelville boundary.

2.2. Carbon and sulfur biogeochemistry

Although changes in carbon isotopes alone can be interpreted in a number of ways, co-variations in paired carbon and sulfur isotopes from multiple paleobasins can be linked to changes in global ocean redox conditions (e.g., Gill et al., 2011a, 2011b; Owens et al., 2013; Edwards et al., 2018; Young et al., 2019). These changes in redox conditions are recorded in marine carbonates as $\delta^{13}C_{carb}$ and $\delta^{34}S_{CAS}$, which will become more positive as the expansion of reducing conditions causes the increased burial of organic carbon and pyrite, respectively.

Organic carbon exported to the seafloor is used as a substrate for anaerobic respiration such as microbial sulfate reduction (MSR). The

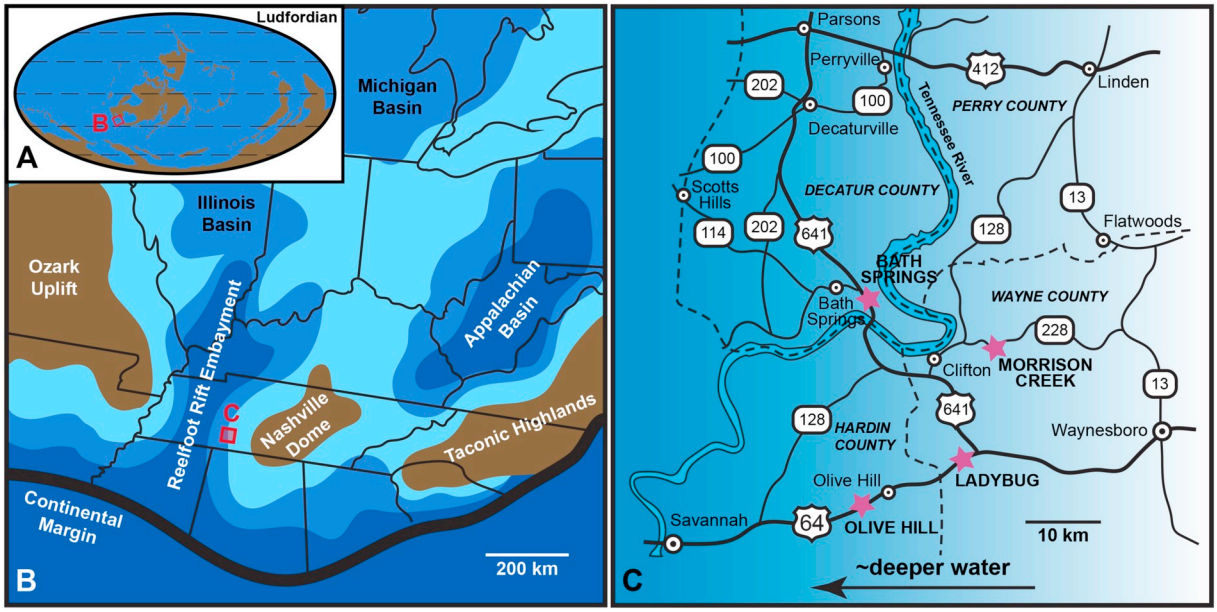

Fig. 1. A) Global paleogeographic map of the late Silurian, ~425 Ma (after Blakey, www2.nau.edu/rcb7). Regional locality indicated by the red square. B) Regional paleogeographic and paleobathymetric map of the southern Laurentian margin and epeiric seaway (modified from Cramer and Saltzman, 2005). Position of locality map marked with red square. C) Locality map of the four study sections with relative paleobathymetry shown with the blue gradient (modified from Barrick et al., 2010). Study sections are labeled and marked by pink stars. (For interpretation of the references to colour in this figure legend, the reader is referred to the web version of this article.)

H_2S produced as a product of MSR reacts with Fe^{2+} to form pyrite (e.g., Canfield et al., 1992). Just as the lighter carbon isotope is preferentially integrated into organic matter during photosynthesis, the lighter sulfur isotopes are preferentially assimilated during MSR and buried as pyrite. This drives seawater sulfate sulfur isotope ($\delta^{34}S_{SO4}$) values heavier as more isotopically light sulfur is removed from the oceans (Bottrell and Newton, 2006). A proxy for capturing ancient seawater sulfate sulfur isotopes is carbonate-associated sulfate, $\delta^{34}S_{CAS}$, as the sulfate anion is substituted into the carbonate crystal lattice with negligible fractionation (Kampschulte et al., 2001; Lyons et al., 2004; Bottrell and Newton, 2006). The modern residence time for sulfur in the oceans is on the order of 10^6 yrs., compared to ocean mixing time of 10^3 yrs., thus $\delta^{34}S_{CAS}$ records are inferred to be a global proxy for the approximate extent of pyrite burial which is most efficient under euxinic marine water columns and/or sulfidic sediment pore waters (e.g., Gill et al., 2011a, 2011b; Owens et al., 2013). While pyrite sulfur isotope, $\delta^{34}S_{pyr}$, records have been shown to parallel the global proxy $\delta^{34}S_{CAS}$ records in some marine settings, these records are often influenced by local factors such as MSR rates, sulfate concentrations, organic matter and Fe availability, and location of pyrite formation, thus reflecting local redox conditions (e.g. Canfield and Thamdrup, 1994; Leavitt et al., 2013; Gomes and Hurtgen, 2015; Sim, 2019).

2.3. I/Ca, a local redox proxy

Iodine to calcium ratios provide a novel proxy to investigate local water-column redox conditions as recorded in carbonate facies (Lu et al., 2010, 2017, 2018; Hardisty et al., 2014, 2017; Zhou et al., 2014, 2015; Owens et al., 2017). Iodine exists in seawater as a reduced species, iodide (I^-), and an oxidized species, iodate (IO_3^-; Wong and Brewer, 1977). The speciation of iodine in seawater is sensitive to water-column oxygen conditions, being one of the first redox-sensitive elements to be reduced under low oxygen conditions (Rue et al., 1997). In well-oxygenated waters, iodine exists almost exclusively as IO_3^-, which is incorporated into carbonate minerals during precipitation (Lu et al., 2010). As oxygen concentrations decrease, IO_3^- is quantitatively reduced to I^-, which cannot be structurally substituted into carbonates (Lu et al., 2010).

As only IO_3^- is incorporated into carbonates, carbonate iodine concentrations can be used as a proxy for water column oxygen conditions, particularly for the early onset of oxygen loss, but the return to more oxic values might be slow due to iodide oxidation rates (as discussed in Hardisty et al., 2020). In the modern ocean, water column mixing and upwelling also play a role in the speciation of iodine (Lu et al., 2019), as was also likely the case for the ancient oceans. Work on the I/Ca proxy in the modern ocean has shown that well-oxygenated settings typically have an I/Ca ratio of greater than 2.6 µmol/mol (Lu et al., 2016). Thus, I/Ca ratios between zero and 2.6 µmol/mol imply that some oxygen must be present, even if in low concentrations (Lu et al., 2010; Owens et al., 2017). This proxy is essentially a qualitative gauge for the position of the oxycline in relation to the environment in which the sediment constituting the analyzed carbonate rock was deposited (Lu et al., 2018). I/Ca ratios are commonly reported as I/(Ca + Mg), as they are herein, to account for variable carbonate mineralogy and particularly dolomitization in ancient carbonates (e.g., Hardisty et al., 2014, 2017; Lu et al., 2017, 2018).

2.4. Microfacies analyses

Detailed facies studies can provide information relating to the depositional environment of sedimentary strata. As carbonate sediments commonly undergo rapid lithification, the internal textural details of limestone beds tend to preserve a faithful record of approximately original synsedimentary characteristics (e.g., Flügel, 2010, and references therein). Together with carbonate textures, which in large part reflect hydrodynamic conditions, the fossil grain assemblages of the rocks can record changes in the depositional environment as these varied with ambient conditions (e.g., Lindskog and Eriksson, 2017). Thus, systematic qualitative and quantitative analyses of abiotic and biotic properties in thin sections (i.e., microfacies) have the potential to tease out invaluable paleoenvironmental information and also provide means for detailed comparisons between sedimentary/stratigraphic successions.

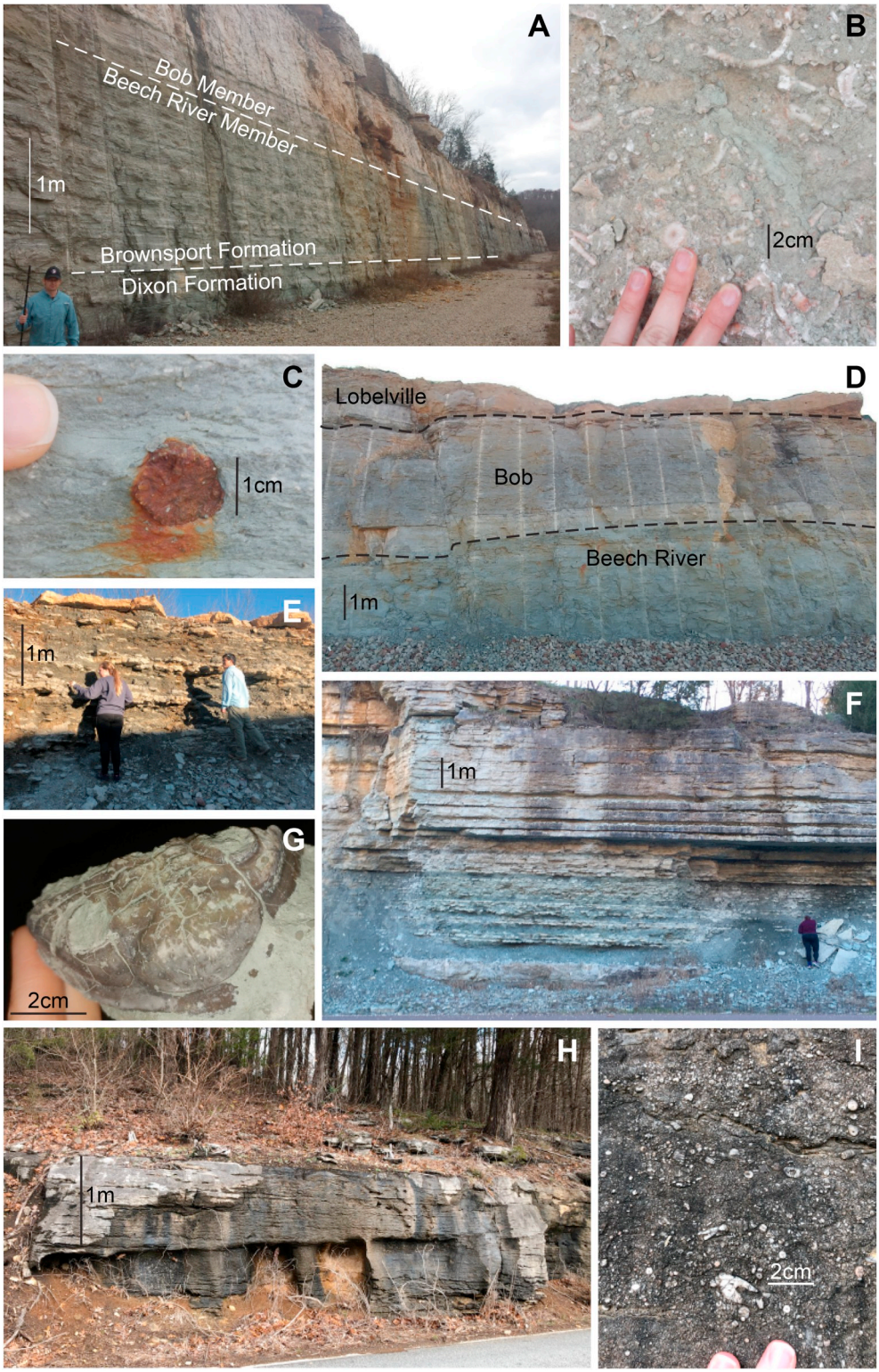

Fig. 2. Representative field photos from the four sections along the Western Tennessee Shelf. A) Dixon and lower Brownsport formations exposed at the lower Ladybug roadcut, dashed lines mark the formational boundary and the boundary between the Beech River and Bob members. B) Encrinite in the Bob Member from the upper Ladybug roadcut. C) Pyrite nodule with iron staining in the Beech River Member at the Olive Hill roadcut. D) Brownsport Fm. exposed at Olive Hill roadcut with dashed lines to mark the boundaries between members. E) Interbedded shales and carbonates of the Lobelville Member at Olive Hill. F) Variably interbedded shales and carbonates in the upper Brownsport Fm. at the upper Bath Springs section. G) Anterior part of an articulated trilobite from the upper Bath Springs roadcut, tentatively identified as *Dalmanites limulurus*. H) Lowest exposure of the Brownsport Fm. at the Morrison Creek section. I) Weathered surface of encrinite from the lower Brownsport Fm. at Morrison Creek.

3. Materials and methods

3.1. Sample preparation

Samples were collected and described in detail every ~0.25–0.5 m from the Morrison Creek, Ladybug, Olive Hill, and Bath Springs sections in western Tennessee (see Supplemental Materials for precise coordinates for all study localities). Where possible, intervals with clear evidence of diagenetic influence, such as secondary calcite veins, pyrite nodules, and/or iron oxide staining, were avoided during sampling (i.e., Fig. 2C, D). Weathered edges and secondary calcite veins were mechanically removed using a water-based diamond blade saw. Representative samples from each section (50–100% of sample series, variable by section) were further slabbed to produce thin sections for the microfacies analyses. From the samples, approximately 1 g of powder was preferentially micro-drilled from micritic matrix (except in the case of grainstones) for $\delta^{13}C_{carb}$ and I/Ca analyses. For all other procedures, the remaining sample was crushed and powdered using an

alumina ceramic disc mill with a SPEX8510 ShatterBox.

3.2. Microfacies point counting and statistics

All thin sections were studied qualitatively and quantitatively to assess the spatiotemporal variability of depositional environments, following the approach of Lindskog and Eriksson (2017). The relative amount of grains in relation to matrix, cement, and remaining voids (i.e., carbonate textures) were determined through point counting using the grain-bulk method of Dunham (1962). A total of 600 points were counted per thin section; for assessing small-scale textural variability, every thin section was counted in sets of two 300-point sessions (each covering approximately half of the sample area). Due to the common complexity and variability in shape of carbonate grains and as their size in carbonates is not necessarily related to hydrodynamic conditions in the depositional environment (e.g., Jaanusson, 1972; Olgun, 1987; Flügel, 2010), grain size was not systematically measured. However, it is commented on below where grain size is perceived as an important detail (see Section 4.1.1).

The fossil grain assemblages of the thin sections were analyzed using a modified form of ribbon counting (see Flügel, 2010), wherein biogenic grains falling within continuous strips ('ribbons') aligned perpendicular to bedding were identified. Six categories were distinguished: Brachiopoda, Bryozoa, Echinodermata, Ostracoda, Trilobita, and Other (minor faunal/floral constituents, and 'problematica'). As is the case for grain abundance, these analyses were subdivided into 300 × 2 counts; counting sessions were halted when 300 grains had been identified. Thus, analyses spanned more data points when including unidentified grains. Such grains typically account for c. 5–10% of the observed grains, but as these have a negligible influence on data trends, for clarity, they were not included in the visual data presentations. Each grain was only counted once and, as different organism groups tend to produce grains of different sizes, the relative abundance of different fossil grain types does not necessarily translate directly into relative rock area/volume.

3.3. Geochemical analyses

For the analysis of carbonate carbon isotopes, 200–300 μg of carbonate powder was weighed and acidified with 100% H_3PO_4 at 25 °C for 24 h. Stable carbon and oxygen isotopes of the evolved CO_2 gas were then obtained using a ThermoFinnigan Gas Bench II Autocarbonate device coupled to a ThermoFinnigan Delta Plus XP isotope-ratio mass spectrometer (IRMS) at the National High Magnetic Field Laboratory (NHMFL) at Florida State University. All carbon and oxygen isotope values are reported in standard delta notation (δ) with units of per mil (‰) relative to the Vienna Pee Dee Belemnite (V-PDB) standard. The analytical precision of $\delta^{13}C_{carb}$ and $\delta^{18}O_{carb}$, based on long-term, replicate analysis of NBS-19 and other lab standards, are ± 0.05‰ (1σ) and ± 0.1‰ (1σ), respectively. Internal standards include the following: ROY-CC (+0.67‰, −12.02‰), MB-CC (−10.5‰, −3.5‰), and PDA (−1.3‰, −5.34‰).

To obtain organic carbon isotopes ($\delta^{13}C_{org}$), sample powder masses were accurately weighed (2–4 g) and then acidified with 6 M HCl to remove carbonate minerals. Insoluble residues were rinsed multiple times in ultrapure (deionized, 18.2 MΩ) water until a neutral pH was achieved and then dried overnight in an oven at 70 °C. Residues were homogenized and weighed into tin cups for analysis. The organic carbon isotope values were measured using a Costech Elemental Analyzer coupled to a ThermoFinnigan DeltaPlus XP IRMS via open-split Conflo III at the NHMFL. Weight percent of total organic carbon (TOC) was then calculated based on the comparison of voltages for the ion beam intensity of mass 44 and the area all integration for masses 44, 45, 46 for CO_2^+ between the unknown samples and the known weight percent carbon of the gravimetric standard acetanilide. Internal carbon isotope standards include: Acetanilide (−29.2‰), Urea-2 (−8.13‰), and Sugar (−12.7‰). Analytical precisions of ± 0.2‰ (1σ) for $\delta^{13}C_{org}$ and ± 0.7% (1σ) for % C are based on long-term, replicate analysis of lab standards calibrated to IAEA standards. Data for $\delta^{13}C_{org}$ and TOC wt % are only reported for the Olive Hill and Bath Springs sections due to extremely low TOC wt% (< 0.03%) associated with the grainstones and packstones of the Morrison Creek and Ladybug sections.

Extractions of carbonate associated sulfate (CAS) for sulfur isotope ($\delta^{34}S_{CAS}$) analysis were performed with minor modifications from procedures outlined by Wotte et al. (2012). Between 80 and 250 g of sample powder was rinsed three times in 10% NaCl solution and three times in ultrapure water (deionized and distilled, 18.2 MΩ) for 12 h per rinse to remove soluble, secondary sulfate minerals. Thereafter, 6 M HCl was titrated into the samples to liberate sulfate from the carbonate matrix; this was done for no more than 2 h per sample in an attempt to avoid pyrite oxidation. Insoluble residues were separated from the acidified solution via centrifugation. The remaining solutions were brought up to a pH of 10 with NaOH and the precipitates from this reaction were removed via filtration. Post-filtration, the remaining solutions were brought to pH 4 using 12 M HNO_3. Excess saturated $BaCl_2$ was added to each sample solution and dissolved sulfate allowed to precipitate as barite ($BaSO_4$) over 72 h. The barite was then rinsed with ultrapure water and dried.

Chromium reducible sulfides (CRS) were extracted from the insoluble residues of the acidification step of the CAS extraction based on modified protocols from Canfield et al. (1986) and Brüchert and Pratt (1996). Residues were reacted with a 70:30 mixture of 12 M HCl and 1 M $CrCl_3$ in an N_2 purged flask. Evolved H_2S gas was then bubbled into $AgNO_3$ to precipitate Ag_2S. The total amount of precipitatant was gravimetrically determined to calculate the concentration of pyrite, assuming quantitative stoichiometry. Approximately 350 μg of barite (CAS) or silver sulfide (CRS) was weighed into tin cups with V_2O_5 for sulfur isotope analysis using a Thermo Isolink Elemental Analyzer coupled via open-split Conflo IV to a Thermo Delta V Plus IRMS at the NHMFL. All sulfur isotope results ($\delta^{34}S_{CAS}$ and $\delta^{34}S_{pyr}$) are reported in standard δ-notation with units reported in ‰ relative to Vienna Cañon Diablo Troilite (V-CDT). The analytical precision, based on long-term, replicate analysis of lab standards calibrated to IAEA standards, is ± 0.2‰ or better (1σ). Samples are calibrated to internal laboratory standards EMR-CP (+0.9‰), PQM2 (−16‰), ERE (−4.7‰), PQB-D (+40.5‰), and SWP (+20.3‰).

I/(Ca + Mg) ratios were measured at the NHMFL using an Agilent 7500cs quadrupole inductively coupled plasma mass spectrometer (ICP-MS) according to standard methods (Lu et al., 2010, 2017; Hardisty et al., 2014, 2017; Zhou et al., 2014, 2015). For brevity, I/(Ca + Mg) is referred to throughout the paper as I/Ca. Approximately 2–5 mg of micro-drilled carbonate powder was used for each analysis, 3% HNO_3 was added to each sample to completely dissolve all carbonate material. Samples were vortexed and centrifuged; the supernatant was then diluted to a ~ 50 ppm Ca + Mg solution. Most samples were diluted in a matrix of 0.5% HNO_3 and 0.5% tetramethyl ammonium hydroxide (iodine-stabilizing solution), some samples were diluted using 2% HNO_3. Based upon replicate analysis of several samples and reference materials there is no notable difference in I/Ca ratio between the two variations of the method. The calibration standards were made each day by serial dilution of a 10 ppm Iodide ICP-MS standard from High Purity Standards and with a similar matrix of ~50 ppm Ca + Mg. The long-term accuracy of this procedure was based on replicate measurements of known reference materials (KL1-2, KL1-4; e.g., Hardisty et al., 2014).

4. Results

4.1. Microfacies

The general petrographic characteristics and interpretations of the depositional environment(s) of the Brownsport Formation and its

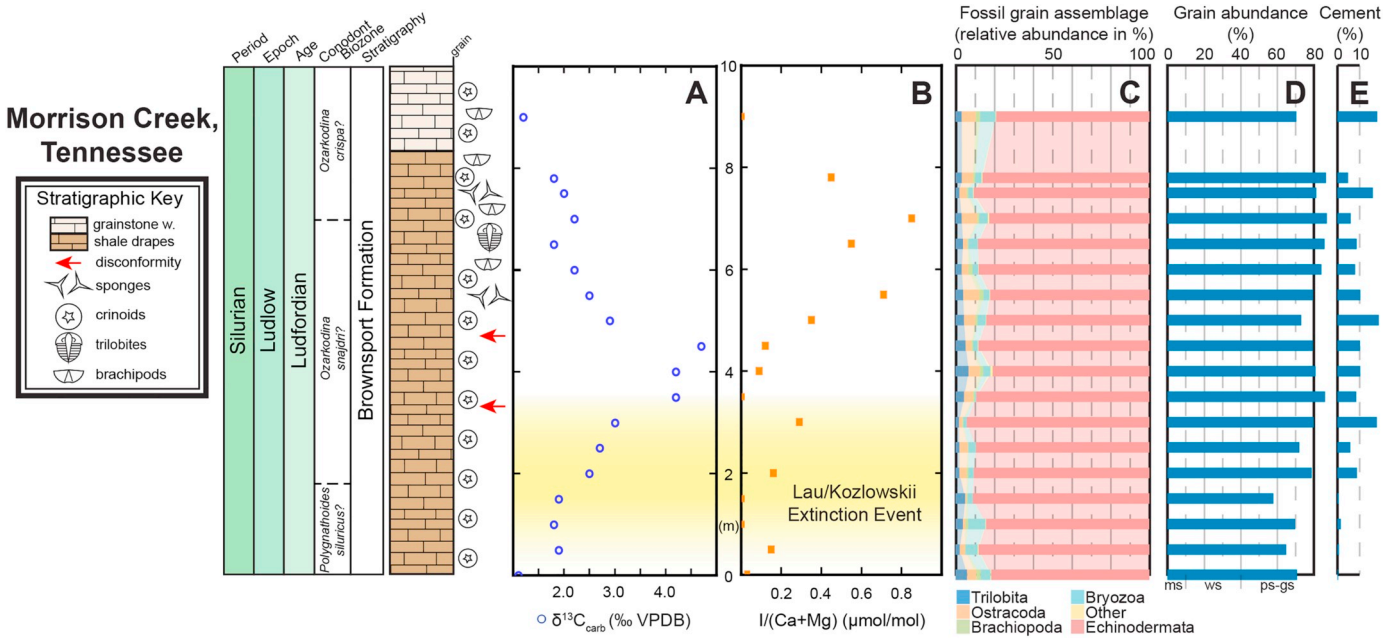

Fig. 3. Stratigraphic column for the Morrison Creek section with geochemical and microfacies data. Conodont biozones after Barrick et al. (2010), Jeppsson (2005), McAdams et al. (2019). The approximate Lau/Kozlowskii extinction interval is shaded in yellow. A) Carbonate carbon isotope data. B) I/(Ca + Mg) ratio data. C) Relative abundances of fossil grains. D) Grain abundance with the approximate divisions for different Dunham (1962) carbonate textures marked. ms: mudstone, ws: wackestone, ps: packstone, gs: grainstone. E) Percentage of cement. References and abbreviations the same for subsequent data figures. (For interpretation of the references to colour in this figure legend, the reader is referred to the web version of this article.)

members, as well as the bounding strata, have been described and discussed in some detail by Broadhead and Gibson (1996). Here, our focus lies on the spatiotemporal variations seen in the study area. The results of the quantitative microfacies analyses are summarized in Figs. 3–6.

4.1.1. *Carbonate textures, fabrics, authigenic minerals, diagenetic artifacts, etc.*

Carbonate textures in thin sections span nearly the entire Dunham scheme, from carbonate mudstone to grainstone, although dominant textures vary both laterally between sections and vertically within (see Dunham, 1962; Flügel, 2010). Broadly from east to west, carbonate microfacies change from consistently coarse-textured (packstone–-grainstone) to finer-textured (mudstone–wackestone, packstone occurs), although there are clear variations throughout individual sections (Figs. 3–7). Overall, the rocks tend to preserve original sedimentary characteristics well, but diagenetic recrystallization effects (calcite, dolomite) occur locally in all studied sections. Obvious artifacts due to large-scale tectonics are essentially absent, but relatively young mm-scale veins filled with calcite and occasionally pyrite occur.

The strata at the Morrison Creek section are typically characterized by very coarse carbonate textures and commonly a near-complete lack of (preserved) carbonate matrix; the proportion of carbonate mud decreases up-section. Relatively mud-rich beds contain sparse bioturbation structures and patches of finely disseminated crypto- and microcrystalline pyrite; sedimentary laminae show deformation around relatively large grains. The interstices between grains typically comprise coarse calcite and occasionally pores; dissolution features and fitted fabrics are common (Figs. 3, 7). Much of the 'cement' is clearly due to secondary recrystallization, as it has commonly affected skeletal grains (mainly echinoderms). Grain assemblages are almost entirely comprised of skeletal grains, but silt-to sand-sized, sub-angular–rounded (see Powers, 1953) quartz is occasionally present. Many beds are cross-bedded internally. Calcareous ooids and putative micro-oncoids occur in the middle part of the succession at Morrison Creek, in association with exceptionally coarse-grained skeletal material and relatively abundant quartz grains (Fig. 7; cf. Broadhead and Gibson, 1996). Many grains in the upper half of the section are discolored due to impregnation with iron oxides (limonite-like compounds).

The overall characteristics of the strata of the Ladybug section are similar to those at the Morrison Creek section, although the proportion of matrix is typically higher and carbonate textures are correspondingly finer (Figs. 4 and 7). Recrystallization effects are less prominent, although can be locally quite severe. Bioturbation (commonly distorted by compaction) is more prevalent in muddy strata, cross-bedding occurs more rarely. Carbonate texture and grain size coarsen into the middle of the section, wherein ooids and micro-oncoid-like grains are locally abundant, but become finer again up-section. This fining is associated initially with discolored grains (~limonite) and higher up in the section, in the upper Bob and Lobelville members, glauconitic grains occur. The latter are sand-sized and typically sub-rounded–rounded; glauconite (sensu *lato*) occurs both as impregnation/pore filling (in skeletal grains) and as discrete grains of unclear affinity/origin (fecal pellets?; e.g., Odin, 1988). The fine-textured strata in the Lobelville Member at the Ladybug section contain relatively abundant finely disseminated pyrite that occasionally forms minute aggregates in the rock matrix and is commonly concentrated in the pores of echinoderm grains.

The Olive Hill section is overall characterized by clearly finer carbonate textures than the previously described strata of the Morrison Creek and Ladybug sections, and many samples are notably argillaceous (Figs. 5 and 7). Lamina-like features in the matrix-rich/argillaceous strata show deformation around relatively large grains. Silt- to fine sand-sized, commonly sub-angular–sub-rounded quartz occurs throughout, especially in relatively argillaceous intervals. Carbonate textures coarsen towards the middle part of the studied succession, particularly in the Bob Member. The coarsest-textured beds contain notable amounts of glauconite and pyrite-impregnated grains. Contrastingly, the coarsest-textured beds are associated with relatively small average grain sizes. The matrix in samples from the upper Bob and Lobelville members is typically densely strewn with silt-sized calcite and dolomite crystals, and microcrystalline calcite permeates some samples. Related recrystallization has had a negative effect on the

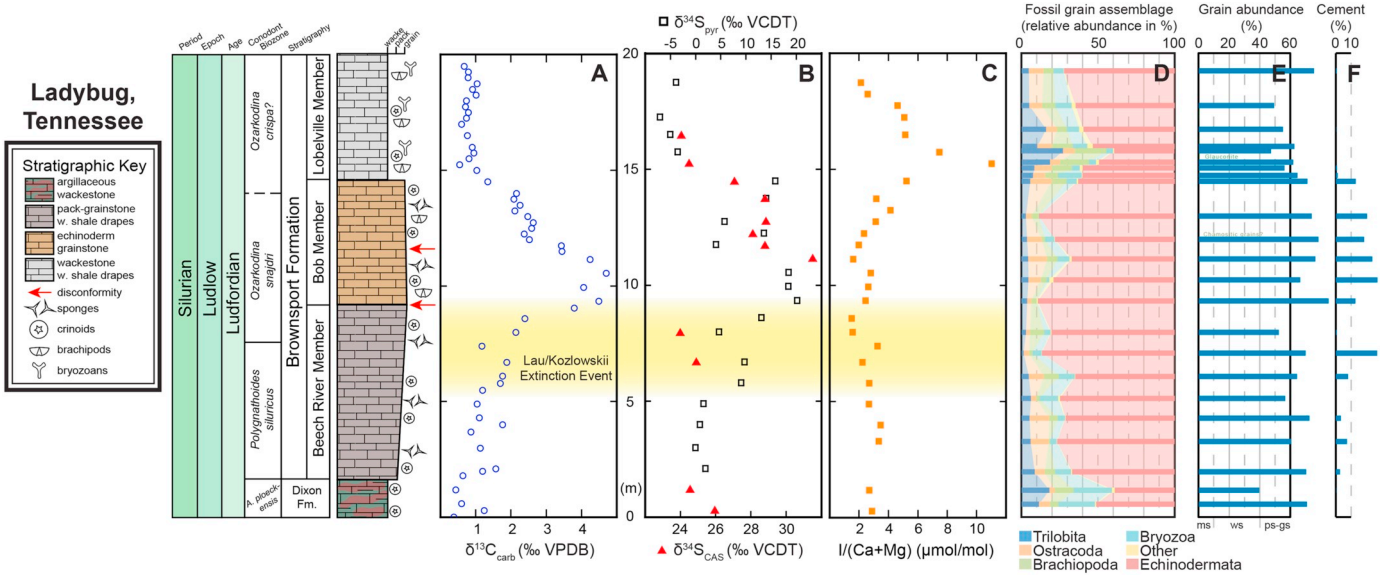

Fig. 4. Stratigraphic column for the Ladybug roadcuts with geochemical and microfacies data. A) Carbonate carbon isotope data. B) Carbonate-associated sulfate and pyrite sulfur isotope data. C) I/(Ca + Mg) ratio data. D) Relative abundances of fossil grains. E) Grain abundance with presence of chamosite and glauconite noted and the approximate divisions for different Dunham (1962) carbonate textures marked. F) Percentage of cement.

preservation of skeletal grains. Carbonate textures become slightly finer again up-section, but the Lobelville Member is generally coarser-textured than the Beech River Member. Pyrite aggregates and finely disseminated pyrite occur throughout the Olive Hill section, but are most common in mud-rich, finer-textured strata.

The strata at the Bath Springs section share many characteristics with those at the Olive Hill section, although dominant carbonate textures tend to be coarser (Figs. 6 and 7). Relatively fine-textured sediments are found near the middle of the succession, but they coarsen up-section (boundaries of stratigraphic members indeterminable; see Supplemental Materials). Glauconitic grains occur sporadically, and sand-sized quartz grains (sub-angular–sub-rounded) are relatively common throughout. Samples from the upper part of the succession commonly show significant recrystallization effects and growth of silt- to sand-sized calcite and dolomite crystals being common components in the rock matrix. This has in part led to 'assimilation' of skeletal grains, which have thus become difficult to discern and identify. Coarse crystallization, locally associated with the formation of pyrite (cf. Lindström, 1984), has also occurred in relatively young fractures in the rock. Pyrite aggregates and finely disseminated pyrite occur throughout the succession at the Bath Springs section but are most abundant in strata with the aforementioned (re)crystallization effects.

4.1.2. Fossil grain assemblages

Echinoderms, ostracods, bryozoans, trilobites, and brachiopods comprise the most common fossil components among skeletal grain assemblages in the studied sections. Other, typically rare, fossil grains include mollusks, sponges (spicules, 'body fossils'), corals, calcareous algae, and 'problematica'. Along with the changes in dominant carbonate textures (see above), fossil grain assemblages show an approximate east–west trend going from entirely echinoderm-dominated to arthropod-rich and varied. Within individual sections, there are commonly distinct variations throughout the studied stratigraphic interval.

At the Morrison Creek section, the skeletal grains assemblages are strongly dominated by echinoderms, but some variations can be confidently detected throughout the studied succession (Figs. 3C and 7). The basal part of the section contains a small fraction of bryozoans and trilobites, with trilobites reaching a peak about mid-way through the section. The upper half of the succession contains a relatively large proportion of ostracods, and bryozoans gradually increase in abundance. Putative calcareous algae occur sporadically throughout.

The Ladybug section shows an overall dominance of echinoderms among fossil grain assemblages, although variations are more pronounced than at the Morrison Creek section (Figs. 4D and 7). From the Dixon Formation and the lower Beech River Member, moving up-section, there is a gradual shift from more varied and 'diverse' faunas, with notable numbers of bryozoans, trilobites, ostracods, and brachiopods, and relatively abundant corals into distinctly echinoderm-dominated assemblages. After echinoderms reach peak abundance (with some variations) in the upper Beech River and Bob members, a trend back towards more varied/'diverse' faunas is observed through the upper Bob and Lobelville members. A distinct temporary acme in trilobites and brachiopods is seen in the lower part of the Lobelville Member.

The strata at the Olive Hill section can broadly be divided into two parts that are characterized by different fossil grain assemblages (Figs. 5D and 7). The Dixon Formation and the Beech River Member host relatively varied and 'diverse' assemblages, with relatively abundant echinoderms, bryozoans, trilobites, and sponges (locally, corals), and the overlying Bob and Lobelville members are characterized by ostracod-rich strata with relatively few bryozoans and echinoderms. A consistent trend of increasingly abundant echinoderms occurs from the Dixon Formation to near the contact between the Beech River and Bob members, where there is an abrupt change in the fossil grain assemblages.

The fossil grain assemblages and their variations at the Bath Springs section are similar to those at the Olive Hill section, although trilobites are consistently more abundant (Figs. 6D and 7). The basal part of the composite section at Bath Springs is characterized by bryozoan-rich fossil grain assemblages, with a trend of increasingly abundant echinoderms up section. The middle part of the succession is unusually rich in sponge spicules. Grain assemblages change markedly in these strata, wherein ostracods and trilobites become relatively abundant. This change occurs mainly at the expense of echinoderms and bryozoans, and especially the latter are notably less abundant in the upper half of this succession.

4.2. Geochemistry

In the Morrison Creek section, $\delta^{13}C_{carb}$ values in the lowest part of the section are ~ + 1.1‰ with maximum excursion values reaching

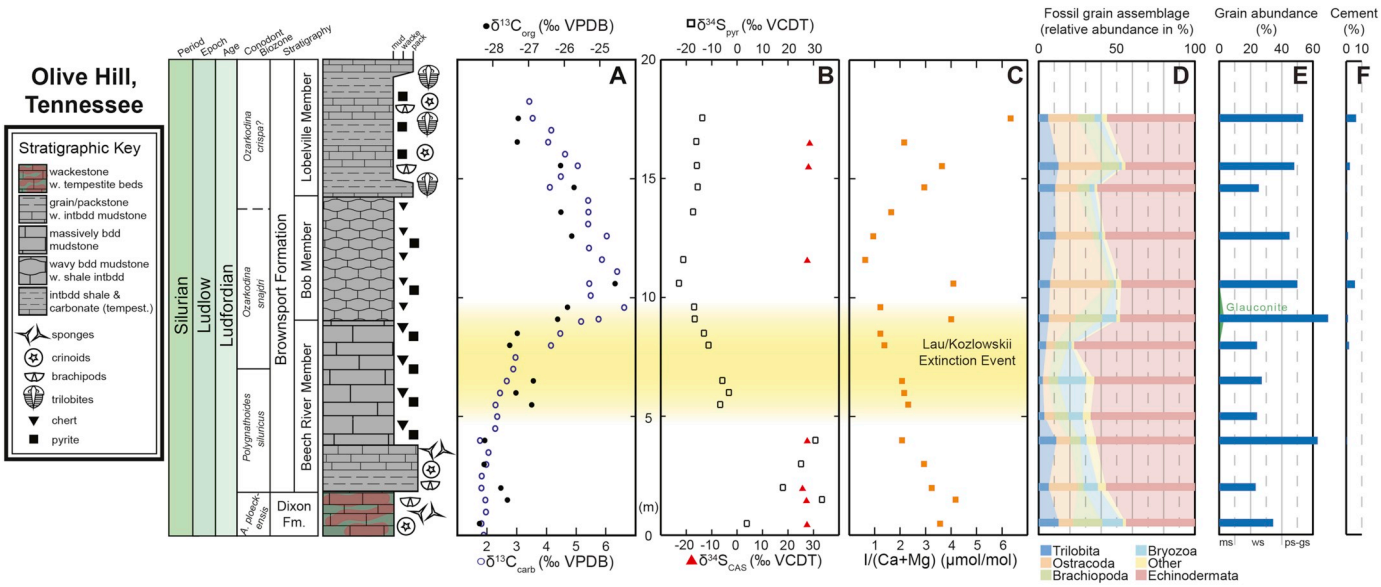

Fig. 5. Stratigraphic column for the Olive Hill roadcut with geochemical and microfacies data. A) Carbonate and organic carbon isotope data. B) Carbonate-associated sulfate and pyrite sulfur isotope data. C) I/(Ca + Mg) ratio data. D) Relative abundances of fossil grains. E) Grain abundance with presence of glauconite noted and the approximate divisions for different Dunham (1962) carbonate textures marked. F) Percentage of cement.

+4.7‰ (Fig. 3A). It is unclear if the entire Lau CIE is captured in this section, as there are little to no baseline values recorded around the CIE at this locality. I/Ca ratios are low throughout this section, < 1.0 μmol/mol (Fig. 3B). Ratios do increase up-section, though, with the lowest values corresponding to the interval just before and during peak values of the CIE, ≤ 0.3 μmol/mol, and highest values during the falling limb of the CIE, 0.4–0.9 μmol/mol.

The Lau CIE is also documented in the Ladybug section, with baseline $\delta^{13}C_{carb}$ values ~ + 1.0‰ and peak excursion values once more at +4.7‰ in the lower Bob Member (Fig. 4A). There is also a positive excursion in the $\delta^{34}S_{CAS}$ data which records a baseline of ~ +24.0‰ in the Beech River Member. Across the peak values of the CIE in the lower Bob Member, $\delta^{34}S_{CAS}$ values increase to +31.5‰ before declining back to baseline values in the overlying Lobelville Member (Fig. 4B). Additionally, $\delta^{34}S_{pyr}$ values parallel the excursion in the $\delta^{34}S_{CAS}$ data, starting at a baseline of ~0‰ in the Beech River Member and reaching peak values of +20‰ coeval with peak values of the CIE in the lower Bob Member, before falling to values as low as −7‰ in the post-excursion baseline within the Lobelville. I/Ca ratios are low, between 1 and 3 μmol/mol, through the Beech River and lower Bob members, coeval with pre-excursion baseline and peak values of the CIE (Fig. 4C). In the middle-upper Bob Member, I/Ca ratios increase to a peak value of 11 μmol/mol in the lowest part of the Lobelville Member as $\delta^{13}C_{carb}$ values are returning to baseline values. I/Ca values then decrease to ~2 μmol/mol through the rest of the measured section.

In the Olive Hill section, the Lau CIE is recorded as parallel excursions in both the $\delta^{13}C_{carb}$ and $\delta^{13}C_{org}$ data (Fig. 5A). The $\delta^{13}C_{carb}$ data has a baseline of ~ + 2‰ and steadily increases through the upper Beech River Member to peak values of ~ + 6.6‰; there is no post-excursion baseline at this locality with values only falling to +3.4‰ at the top of the section in the Lobelville Member. The $\delta^{13}C_{org}$ data follows a similar pattern, starting at a baseline of ~ − 28‰, increasing to peak values of −24.6‰ before declining to values of ~ − 27‰. There is a small positive shift in $\delta^{34}S_{CAS}$ from values of ~ + 26 to +28‰ from the lower to the upper part of the section (Fig. 5B). The $\delta^{34}S_{pyr}$ values are high, ~ + 20 to +30‰, in the upper Dixon Formation and lower Beech River Member. In the middle Beech River Member $\delta^{34}S_{pyr}$ values decrease dramatically from +30.7 to −6.6‰ and remain low, between −3.3 and − 22.8‰, through the rest of the section. I/Ca ratios are relatively high, around 3–4 μmol/mol, in the upper Dixon Formation and values fall throughout the Beech River Member (Fig. 5C). Through the rising limb and peak values of the CIE ratios decrease to 1–2 μmol/mol, aside from two seemingly anomalous data points during the peak of the CIE at ~4 μmol/mol. I/Ca ratios steadily increase from a low of 0.6 μmol/mol, coincident with the peak of the CIE, to a peak of 6.3 μmol/mol at the top of the section, coincident with the falling limb of the CIE.

The Lau CIE is documented in the Bath Springs composite section in both $\delta^{13}C_{carb}$ and $\delta^{13}C_{org}$ records (Fig. 6A). The $\delta^{13}C_{carb}$ values begin at a baseline of ~ + 1.0‰ in the lower section and increase to values of ~ + 3.2‰ in the middle section. The upper section records peak CIE values of +7.0‰ at the base and, continuing up-section, values fall back to post-CIE baseline values of ~ + 1.0‰ near the top of the section. The $\delta^{13}C_{org}$ values follow a similar pattern, with values of ~ − 27.5‰ in the lower roadcut increasing to ~ − 26.3‰ in the middle section, and then peak- to post-excursion baseline values of ~ − 25 to −29‰ in the upper section. There is a parallel excursion in $\delta^{34}S_{CAS}$ which begins with baseline values of ~ + 25‰ with possible peak values of ~ + 29.5‰ in the upper section that then fall back to +23 to +24‰ close to the top of the section (Fig. 6B). There is a corresponding, though much higher magnitude excursion in the $\delta^{34}S_{pyr}$ data with pre- and post-excursion baselines of ~ − 30 and ~ −15‰, respectively, and peak excursion values of +38‰. I/Ca ratios follow a similar trend to the Morrison Creek and Ladybug sections. Through the lower part of the section ratios are low, < 1 μmol/mol, except for two outliers (Fig. 6C). However, in the uppermost 7.5 m of the section, during the end of the falling limb of the CIE and return to baseline $\delta^{13}C$ values, I/Ca ratios increase to values as high as 3.7 μmol/mol and shift back to 2.0 μmol/mol near the top of the composite section.

5. Discussion

5.1. Facies and paleoenvironmental development

Overall, the lithologic and sedimentologic data documented herein agree with the generalized descriptions of the Brownsport Formation provided by Broadhead and Gibson (1996; see further references therein), but it is clear the details of macroscopic and microscopic characteristics vary throughout the study area. Notably, the Bob Member commonly appears difficult to identify for practical purposes,

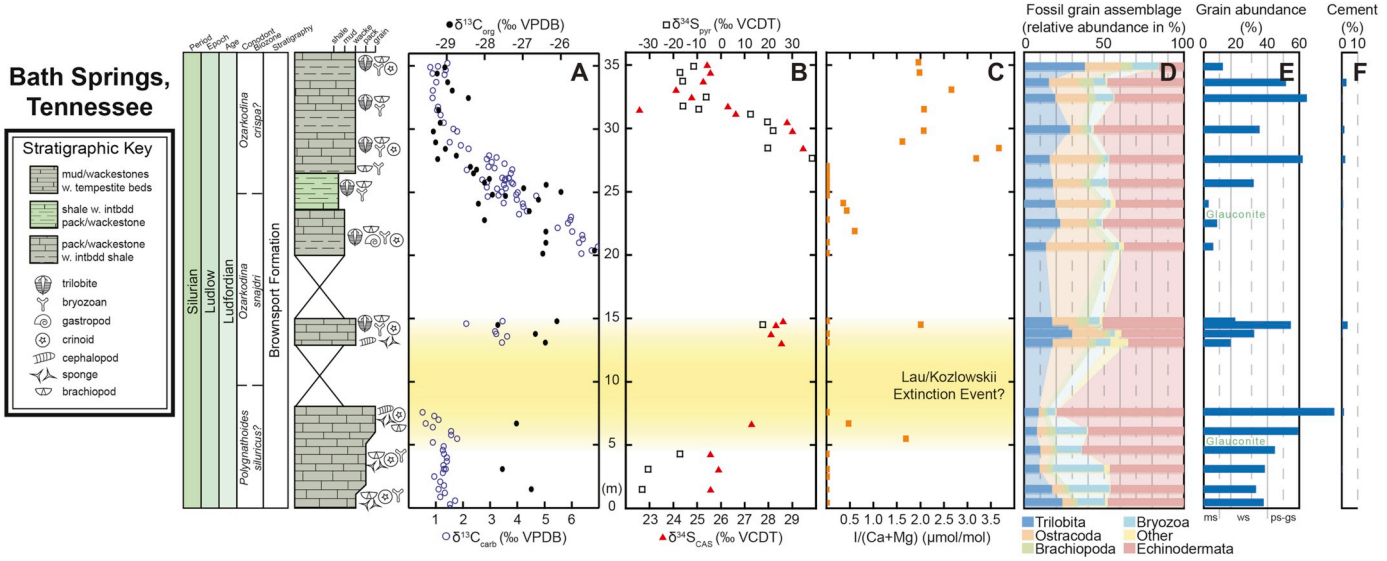

Fig. 6. Composite stratigraphic column for the Bath Springs roadcuts with geochemical and microfacies data. A) Carbonate and organic carbon isotope data. B) Carbonate-associated sulfate and pyrite sulfur isotope data. C) I/(Ca + Mg) ratio data. D) Relative abundances of fossil grains. E) Grain abundance with presence of glauconite noted and the approximate divisions for different Dunham (1962) carbonate textures marked. F) Percentage of cement.

as its character changes significantly with depth along the carbonate shelf (see Section 2.1; Supplemental Material). Broadly, the fossil grain data appear to reflect changes in the macrofossils (see Pate and Bassler, 1908; Amsden, 1949; Broadhead and Gibson, 1996; Barrick et al., 2010), but absolute and relative numbers are commonly offset. This is expected, as different taxonomic groups produce diverse amounts of skeletal material throughout their lifetimes and yield variably sized 'typical' grains (as well as more and less conspicuous macrofossils; cf. Jaanusson, 1972; Lindskog and Eriksson, 2017). Spatiotemporal variations in the fossil (grain) assemblages likely reflect variations in the depositional environment(s) via the life modes and preferences of different taxonomic groups. Substrate characteristics, which are governed by, for example, siliciclastic input, hydrodynamic conditions and/or water depth, likely played a large role; broadly, echinoderms appear to reflect relatively firm substrates, whereas ostracods and trilobites appear to reflect soft substrates (see Section 4.1.2). Local marine redox conditions and the relative position of the chemocline may also have been an important influence on substrate characteristics. For example, oxygenation at the seafloor has strong effects on habitability (e.g., Vaquer-Sunyer and Duarte, 2008).

The spatial variations in the abiotic and biotic components of macro- and microfacies characteristics throughout the study area are consistent with previously reconstructed bathymetric conditions during the Silurian (Fig. 1B, C; e.g., Braille et al., 1984; Broadhead and Gibson, 1996; Cramer and Saltzman, 2005 and references therein). As such, the collective data suggest increasingly deeper water approximately from east to west (present-day directions), reflected broadly through increasingly finer-textured, argillaceous strata and changes in the overall composition of fossil grain assemblages in this direction. Although details vary slightly between localities, the vertical changes in facies through the Brownsport Formation indicate an initial shallowing through the Beech River and basal Bob members, followed by deepening and renewed establishment of relatively stable conditions, corroborating observations of previous studies in Tennessee (e.g. Pate and Bassler, 1908; Broadhead and Gibson, 1996; Barrick et al., 2010). This is consistent with global scenarios, and the collective data suggest that eustatic sea level had an important influence on the overall development during the LKE interval (e.g., Kaljo et al., 1997; Wingforss-Lange, 1999; Calner, 2005; Martma et al., 2005; Jeppsson et al., 2007; Lehnert et al., 2007; Munnecke et al., 2010; Spiridonov et al., 2017).

Barrick et al. (2010) noted that no massive ecologic collapse or obvious 'crisis' appears to have occurred among the macrofauna in the Western Tennessee Shelf through the LKE interval, as has been documented globally from other localities (e.g., Bowman et al., 2019 and references therein). However, the Lau conodont extinction was tentatively recognized within the Brownsport Formation (Barrick et al., 2010). The new data herein of fossil grain assemblage composition for each section clearly shows that within the approximate LKE interval distinct changes among marine communities are recorded along the Laurentian margin. This suggests ecological reorganization in response to changes in the marine environment, possibly related to sea level and/or local redox conditions (see Section 5.3 below). The overall changes in the macro-, micro- and biofacies during the LKE-equivalent and Lau CIE interval closely resemble those in the Lau extinction 'type area' on Gotland, Sweden (see Cherns, 1983; Calner, 2005, Fig. 2; Eriksson and Calner, 2005), as well as those in northeastern Australia (Jeppsson et al., 2007). In tandem with sedimentary characteristics suggesting changes in sea level/water energy, the fossil grain assemblages record a transition from varied ('healthy') pre-event faunas into restricted ('stressed') faunas through the extinction interval and CIE, and returning to a baseline of more varied faunas in the post-event strata. Notably, however, the compositions of post-event fossil grain assemblages differ distinctly from those pre-event, indicating that ambient environmental conditions returned to a new baseline (or/and that the fauna did not recover completely) within the studied time interval. The unusually prevalent ooids and micro-oncoids in the CIE interval of the Morrison Creek and Ladybug sections suggest that 'anachronistic' facies developed up-ramp, in the area that would be most impacted by a decrease in sea level (cf. Calner, 2005; Barrick et al., 2010).

The collective microfacies results indicate that the distinct changes in skeletal grain assemblages are a local expression of the LKE. Assuming that sea level played a significant role in the sequence of events, along with marine redox conditions (see Section 5.3 below), the relatively deep/distal/marginal placement of the study area on the West Tennessee Shelf likely acted to buffer against the most severe effects of the LKE. This may help explain the lack of immediately obvious effects on the macrobiota locally (cf. Barrick et al., 2010). However, in this regard, it should be noted that detailed paleontological studies (within modern taxonomic frameworks), similar to those from Baltica and Gondwana (see Section 1 above), are generally lacking from the Western Tennessee Shelf area. Hence, future, in-depth studies of various macrofossil groups from this area are bound to add important

biodiversity information and ultimately refine the global picture of the biotic development during the LKE and the Lau CIE.

5.2. Diagenesis and the nature of geochemical signals

Post-depositional processes affect all strata to some degree and these processes have the potential to alter primary textures and geochemical signatures. Most samples show limited signs of any obvious detrimental (~late) diagenetic influence in thin sections, but where it occurs it is mainly in the form of recrystallization of carbonate matrices and growth of discrete dolomite rhombs (see Section 4.1.1; cf. Broadhead and Gibson, 1996; Barrick et al., 2010). Complete obliteration of original rock textures was not observed in any sample. There is a tendency in the sampled sections for finer-textured and -grained, i.e. relatively matrix-rich and argillaceous, strata to be more impacted by diagenesis (Figs. 3–7). This can in part be explained by the relative rate of lithification and effective closure of the strata to diagenetic influence in low-temperature regimes. The relatively slow lithification and common susceptibility to compaction of carbonate-poor strata likely exacerbates diagenetic influence, whereas relatively rapid lithification of carbonate-rich strata promotes the preservation of original rock characteristics (e.g., Bathurst, 1987; Flügel, 2010). The overall physicochemical characteristics of the rocks thus in part govern the relative prevalence of diagenetic artifacts.

Overall, diagenetic processes appear to have had little effect on the geochemical proxies; the consistency in stratigraphic trends between localities indicates that the data record primary signals. As also noted by Barrick et al. (2010), despite certain intervals and sections representing quite hydrodynamically (and correspondingly geochemically) active environments, possible reworking seems to have had a negligible effect on bulk elemental and isotopic geochemistry. Conodonts consistently show colour alteration indices of ~1–1.5 (J. Barrick, *pers. comm.*), indicating limited thermal influence on the studied strata (Epstein et al., 1977). Regardless, it is essential to assess whether geochemical signals are reflective of primary seawater conditions or diagenetic alteration (e.g., Banner and Hanson, 1990; Railsback et al.,

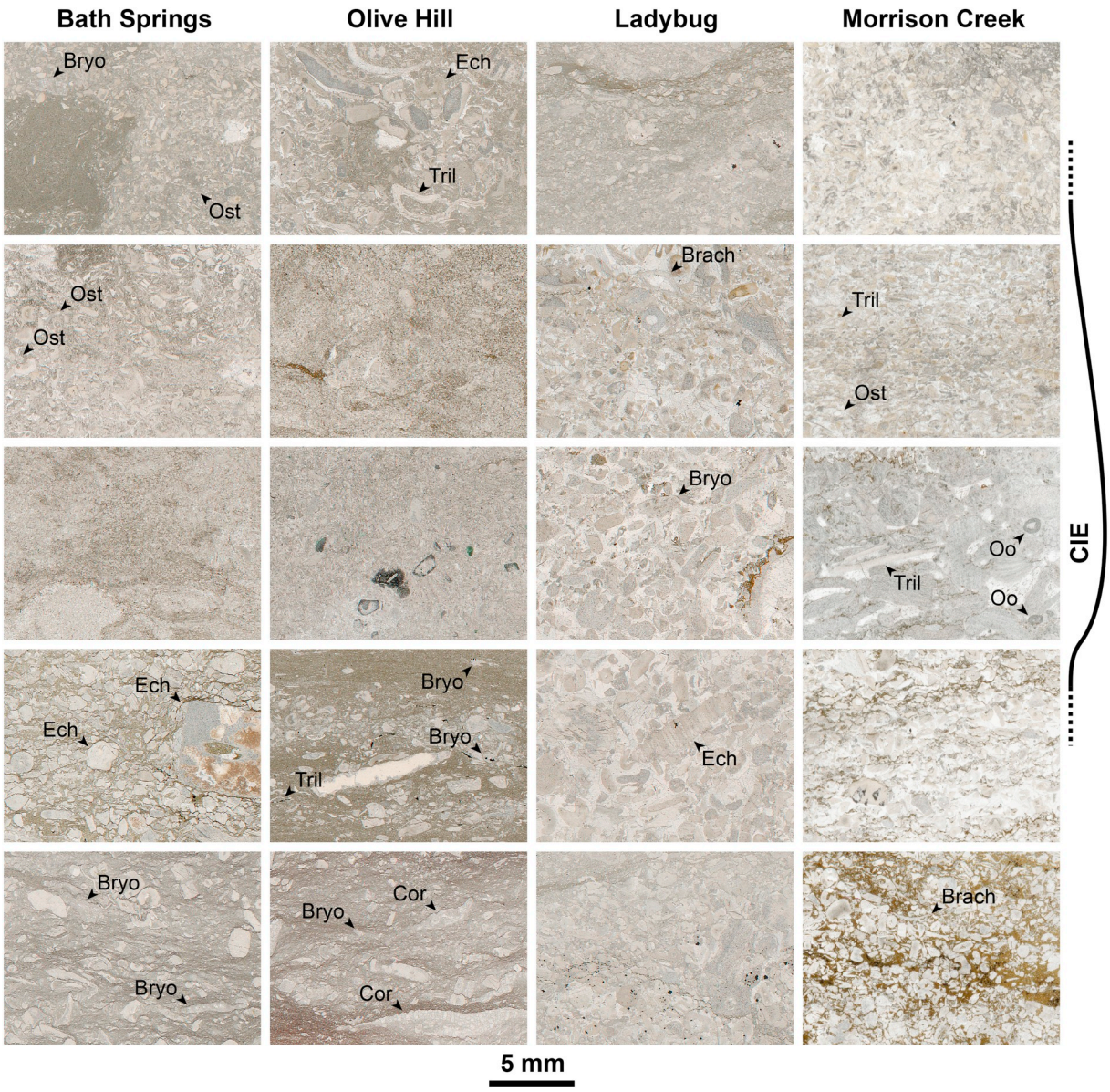

Fig. 7. Representative thin sections showing the lateral and stratigraphic variations in microfacies (images arranged in stratigraphically correct order). A selection of characteristic sediment-forming grains in the sand-sized fraction are indicated: brachiopods (Brach), bryozoans (Bryo), corals (Cor), ostracods (Ost), ooids/micro-oncoids (Oo), and trilobites (Tril).

2003; Gill et al., 2008). Linear relationships observed in cross plots of geochemical data have been extensively used to determine the degree of diagenetic alteration since deposition (e.g., Cramer and Saltzman, 2005; Swart and Eberli, 2005; Gill et al., 2008; Jones and Fike, 2013). Notable correlation between $\delta^{13}C_{carb}$ and $\delta^{18}O_{carb}$ commonly indicates the partial resetting of carbon and oxygen isotope values from meteoric fluid flow. A cross plot of our $\delta^{13}C_{carb}$ and $\delta^{18}O_{carb}$ data (Fig. 8A) shows no significant correlation for any of the four data sets ($r \leq 0.21$, $p > .01$, n: 18–98).

The concentrations of both sulfate and iodate in the carbonate crystal lattice have been shown to decrease during alteration because meteoric fluids have lower concentrations of both anions compared to the original calcite and, particularly in the case of iodate, the flow of reducing fluids can accelerate this process of diagenetic loss (Gill et al., 2008; Sim et al., 2015; Hardisty et al., 2017). To assess the possible meteoric alteration of I/Ca data, the data was plotted against $\delta^{18}O_{carb}$ (Fig. 8B). No significant correlation was observed between I/Ca and $\delta^{18}O_{carb}$ for any of the four data sets ($r \leq 0.22, p > .01$, n: 15–33). The strata at the Ladybug and Olive Hill sections appear to have fared best in terms of preserving original synsedimentary geochemical signals of I/Ca ratios, followed by the Morrison Creek section, whereas the data from the Bath Springs section have been notably altered. In many cases, I/Ca values appear to be 'reset' (i.e. at ~0; Fig. 6C) at the lattermost locality, and this is clearly related to recrystallization effects in the matrix and the prevalent calcite-filled cracks in the section. Given the easy remobilization of iodine-related ions (see Section 2.3), the I/Ca proxy is sensitive to relatively minor diagenetic alteration. This resetting of I/Ca values is likely due to reducing conditions in the pore fluids through the heavily interbedded carbonates and shales of the Bath Springs section, which would be preferentially enriched in the reduced species of iodide. Although diagenetic alteration of the iodine contents has possibly occurred at the Bath Springs section, the overall trend in the data throughout this section is remarkably similar to the other nearby study sections. This suggests that the overall trend in the dataset may still be useful as a qualitative measure that records the local redox conditions at this site. Post-depositional dolomitization can also artificially increase I/Ca ratios if Mg is not accounted for, thus all data presented herein are I/(Ca + Mg) ratios (e.g. Hardisty et al., 2017). Meteoric diagenesis is known to decrease CAS concentrations, but there are little to no known effects on $\delta^{34}S_{CAS}$ values (Gill et al., 2008; Sim et al., 2015). The absence of correlation between $\delta^{18}O_{carb}$ and [CAS] (Fig. 8C; $r \leq 0.29$, $p > .01$, n: 7–36) or $\delta^{18}O_{carb}$ and $\delta^{34}S_{CAS}$ (Fig. 8D; $r \leq 0.28$, $p > .01$, n: 7–30) in the data from the Ladybug, Olive Hill, and Bath Springs sections suggests that $\delta^{34}S_{CAS}$ values have not been markedly reset by meteoric diagenesis.

Contamination via sedimentary pyrite oxidation can also have a significant impact on $\delta^{34}S_{CAS}$ records. Pyrite can be oxidized during later stages of diagenesis or through the chemical extraction of CAS from samples, falsely lowering $\delta^{34}S_{CAS}$ values (Wotte et al., 2012). Linear correlations between $\delta^{34}S_{CAS}$ and $[S_{pyr}]$ or $\delta^{34}S_{pyr}$ have been used as indicators of contamination of sulfate sulfur isotopes from pyrite oxidation. Care was taken to avoid rock with visible (and clearly secondary) pyrite during field collection. Based on our CRS extraction yields, however, pyrite concentrations were high in all four sections, with concentrations as high as 2300 ppm in the Bath Springs section and 1500 ppm in the Ladybug section. Additionally, pyrite was nearly ubiquitous in all the thin sections. Samples with $[S_{pyr}] > \sim 250$ ppm were not considered for CAS as the likelihood of pyrite contamination is greatly increased at higher concentrations (Marenco et al., 2008). The $\delta^{34}S_{CAS}$ data from the Ladybug, Olive Hill, and Bath Springs sections showed low to moderate correlations in cross plots of $\delta^{34}S_{CAS}$ vs. $[S_{pyr}]$ (Fig. 8E), but p-tests found these to be insignificant ($r \leq 0.52, p > .01$, n: 7–30). Correlation of $\delta^{34}S_{CAS}$ vs. $\delta^{34}S_{pyr}$ was also moderate for these three sections (Fig. 8F); the correlations for the Ladybug and Olive Hill sections were not significant ($r \leq 0.62$, $p > .01$, n: 7–8) but the correlation for the Bath Springs section was significant ($r = 0.56, p < .01$, n: 22). This indicates that there could have been some contamination of our reported $\delta^{34}S_{CAS}$ values via pyrite oxidation for the samples from the Bath Springs section, and perhaps the Ladybug and Olive Hill sections to a lesser extent. The net overall effect of this potential pyrite contamination is a shift towards isotopically lighter $\delta^{34}S_{CAS}$ values at these sections, as corresponding $\delta^{34}S_{pyr}$ values at all sections are 7‰ – 61‰ lighter than the coeval $\delta^{34}S_{CAS}$ values. Similar to the iodine discussion above for the Bath Springs section, the overall high concentrations of pyrite in all of our study sections suggest that the trends in our $\delta^{34}S_{CAS}$ datasets are at a minimum useful as a qualitative gauge on changes in global sulfur cycling, especially compared to other less altered sections (see discussion below). Overall, each study section has its own distinctive diagenetic history, but the effects of diagenesis seen along the Western Tennessee Shelf do not preclude the interpretation of primary seawater signatures from our geochemical datasets. The consistentancy of geochemical trends between our study sections from Laurentia and datasets from other paleobasins (e.g., Baltica, Bowman et al., 2019) suggests we can reasonably interpret local to global marine redox conditions.

5.3. Marine redox conditions of the Western Tennessee Shelf

Local redox conditions vary both across the Western Tennessee Shelf and through time as the LKE and Lau CIE progressed globally; this variation included not only water column conditions but also changes in the sediment porewaters (Fig. 9). There is geochemical evidence for distinct changes in local water column oxygenation throughout the LKE and Lau CIE interval, as interpreted from I/Ca ratios. During deposition of the upper Dixon/lower Brownsport formations, prior to the Lau CIE, I/Ca ratios were 3 to 4 μmol/mol (Ladybug and Olive Hill sections), indicating a reasonably well-oxygenated water column locally, notably greater than most Paleozoic I/Ca values and are comparable to previously reported Cenozoic values (Lu et al., 2018). Moving into the extinction interval and corresponding with the rising limb of the Lau CIE, I/Ca ratios decreased to as low as 0.6 to 1.6 μmol/mol at the peak of the CIE (Figs. 4C and 5C; Supplementary Tables S2, S3). During this time period, throughout the deposition of the upper Beech River and the Bob members, water column oxygen contents dropped, though remaining above non-zero values (see Lu et al., 2010; Owens et al., 2017). This is likely indicative of low oxygen or intermittent anoxia in the mid-shelf area. During the falling limb of the Lau CIE, I/Ca ratios increased substantially, reaching a peak of between 6 and 11 μmol/mol in the lower Lobelville Member (Figs. 4C and 5C); the highest I/Ca values correspond to the shallower, and likely more oxygenated, part of the shelf at the Ladybug section. This suggests that local water column oxygen contents not only increased but surpassed what they had been prior to the Lau CIE. The antithetical relationship between I/Ca and $\delta^{13}C$ during the positive carbon isotope excursion at the Ladybug and Olive Hill sections can also be seen in Cretaceous OAE2 records (Lu et al., 2010; Zhou et al., 2015), although generally without the large increase in water column oxygenation post-event. The I/Ca data analyzed from the other two sections cannot be as clearly interpreted. At the Morrison Creek section (Fig. 3C), this same general trend was evident, but the change in I/Ca ratios across the measured interval are suppressed significantly. This could possibly be due to post-depositional IO_3^- loss as a result of the extremely porous nature of the samples from this section (Hardisty et al., 2017). Based on evidence from the carbonate microfacies analyses (i.e., carbonate textures, fossil content, and abundant sand grains and ooids/oncoids) the Morrison Creek section represents the shallowest-water deposition of the four sections. This hydrodynamically active environment should correspondingly have been the most oxygenated, when interpreted in the context of the Ladybug and Olive Hill sections, and thus it is unlikely that the data from the Morrison Creek section represent primary seawater values. At the Bath Springs section, I/Ca values are predominantly zero throughout the lower to middle portions of the section, implying either intermittent

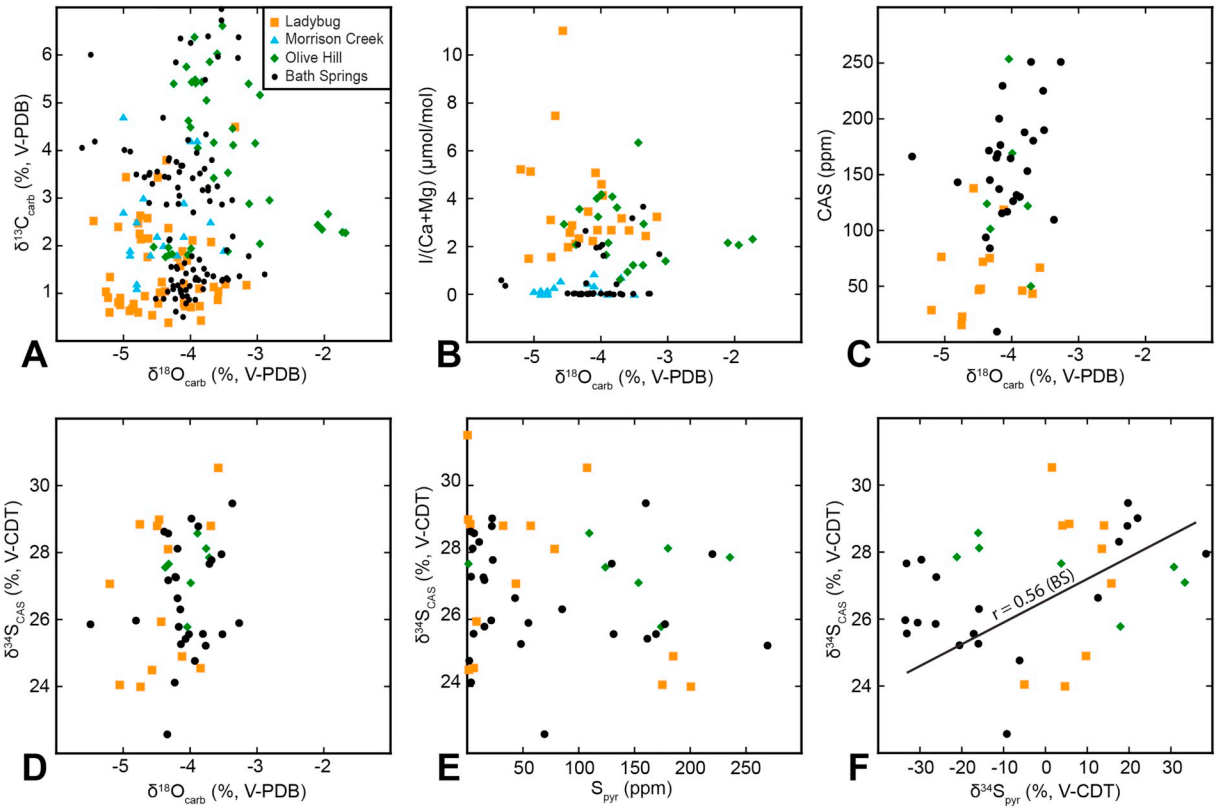

Fig. 8. Cross plots for the assessment of possible diagenetic alteration of carbon, oxygen, and sulfur isotopes, diagenetic alteration of I/Ca ratios, and sedimentary pyrite oxidation at each section (see Section 5.2 for discussion). A) $\delta^{18}O_{carb}$ vs. $\delta^{13}C_{carb}$ (Morrison Creek: $r = 0.14$, $p > .05$, $n = 18$; Ladybug: $r = 0.022$, $p > .05$, $n = 50$; Olive Hill: $r = 0.21$, $p > .05$ $n = 38$; Bath Springs: $r = 0.088$, $p > .05$, $n = 98$). B) $\delta^{18}O_{carb}$ vs. I/Ca (MC: $r = 0.29$, $p > .05$, $n = 15$; LB: $r = 0.20$, $p > .05$ $n = 23$; OH: r = 0.21, $p > .05$, $n = 20$; BS: r = 0.20, $p > .05$, $n = 33$). C) $\delta^{18}O_{carb}$ vs. [CAS] (LB: $r = 0.30$, $p > .05$, $n = 23$; OH: $r = 0.27$, $p > .05$, $n = 7$; BS: $r = 0.17$, $p > .05$, $n = 36$). D) $\delta^{18}O_{carb}$ vs. $\delta^{34}S_{CAS}$ (LB: $r = 0.15$, $p > .05$, $n = 12$; OH: r = 0.27, $p > .05$, $n = 7$; BS: $r = 0.28$, $p > .05$ $n = 30$). E) [S_{pyr}] vs. $\delta^{34}S_{CAS}$ (LB: $r = 0.52$, $p > .05$, $n = 12$; OH: $r = 0.16$, $p > .05$, $n = 7$; BS: r = 0.16, $p < .05$, $n = 30$). F) $\delta^{34}S_{pyr}$ vs. $\delta^{34}S_{CAS}$ (LB: $r = 0.49$, $p > .05$, $n = 8$; OH: $r = 0.62$, $p > .05$, $n = 7$; BS: $r = 0.56$, $p < .01$, $n = 22$).

anoxia (as opposed to low-oxygen conditions) or loss of IO_3^- due to reducing pore fluids (see Sections 4.1.1 and 5.2; Hardisty et al., 2017). Based on changes in lithology (see Supplemental Material) and trends in the $\delta^{34}S_{pyr}$ data (see below) from Bath Springs, reducing water column conditions can still be interpreted with confidence. During the falling limb of the Lau CIE at Bath Springs, I/Ca ratios increase markedly up to 3.5 μmol/mol in the same stratigraphic interval where highest values are recorded from all other sections. Thus, the trend to more oxic conditions post-CIE is similar for all the sections investigated.

Trends in the pyrite sulfur isotope record ($\delta^{34}S_{pyr}$) suggest a number of changes in the redox landscape of the Western Tennessee Shelf. High-magnitude, positive excursions in $\delta^{34}S_{pyr}$ are documented in two of the three sections from which pyrite sulfur isotopes were analyzed (Figs. 4B and 6B). These excursion records (magnitudes of ~ +20‰ at the Ladybug section and ~ +68‰ at the Bath Springs section) are comparable to the +40‰ magnitude $\delta^{34}S_{pyr}$ excursion recorded in coeval strata from Latvia and parallel the +30‰ magnitude $\delta^{34}S_{CAS}$ excursion documented in Gotland (Bowman et al., 2019) and from the Western Tennessee Shelf (see Section 5.4). The $\delta^{34}S_{pyr}$ excursion in sedimentary pyrite paralleling that of $\delta^{34}S_{CAS}$ indicates that the sedimentary pyrite sulfur isotope record at the Ladybug and Bath Springs sections reflect the global sulfate value as pyrite was likely formed in an open system either in a reducing water column and/or near the sediment–water interface and was extensively buried (Gomes and Hurtgen, 2015; Young et al., 2019). Thus, these two $\delta^{34}S_{pyr}$ records are indicators of a global expansion of euxinia and resultant enhanced pyrite burial (see Section 5.4, Bowman et al., 2019). However, the Olive Hill $\delta^{34}S_{pyr}$ dataset does not correspond to any of these other $\delta^{34}S_{pyr}$ records; this sulfur isotope dataset and sedimentary evidence are interpreted to represent local closed-system microbial sulfate reduction. There are no notable positive excursions in either $\delta^{34}S_{pyr}$ (~ −40‰ shift) or $\delta^{34}S_{CAS}$ (~ +2‰ shift) in this section, likely due to local processes overprinting the sulfur isotope records. In the lowest part of the Olive Hill section $\delta^{34}S_{pyr} \geq \delta^{34}S_{CAS}$ (Fig. 5B), indicating that sulfate concentrations at the time and place of sedimentary pyrite formation were low—pyrite was likely being formed in a closed system within sediment porewaters (Fig. 9D; Ries et al., 2009; Gomes and Hurtgen, 2013, 2015). This pyrite isotope data suggests that even though the overlying water column was oxygenated pre-CIE, based on the Olive Hill I/Ca data, the sediment pore waters were reducing. Furthermore, the large negative shift in $\delta^{34}S_{pyr}$ (~ −40‰) in the lower/middle Beech River Member at Olive Hill is most likely indicative of a shift in the primary location of local pyrite formation (Gomes and Hurtgen, 2015). The negative shift and the resulting increase in $\Delta^{34}S$ (= $\delta^{34}S_{CAS}$ - $\delta^{34}S_{pyr}$) suggest that the majority of the pyrite preserved in the upper part of the Olive Hill section formed in the water column, likely near the oxic-euxinic interface (i.e. chemocline; Gomes and Hurtgen, 2015). It is possible that this isotopic shift at the Olive Hill section is also closely tied to the encroachment of oxygen-deficient waters and the sudden availability of reactive iron (Gomes and Hurtgen, 2015).

Pyrite is nearly ubiquitous throughout the four measured and analyzed sections of the Western Tennessee Shelf, whether finely disseminated or nodular. This necessitates major changes to at least sediment porewater redox conditions, if not the water column, in order to generate the sulfide necessary for pyrite formation. Although the Lau CIE was likely caused by increased global carbon burial (Bowman et al.,

2019), carbonate shelves are characteristically oligotrophic, and organic-rich sedimentation was minimal in the sampled area of the Western Tennessee Shelf, likely acting as a limiting factor in the formation of pyrite. In the shallow shelf settings (the Morrison Creek and Ladybug sections) the total organic carbon contents were so low (TOC wt% < 0.03%) that $\delta^{13}C_{org}$ values could not be reliably determined. Along the more argillaceous, deeper shelf (the Olive Hill and Bath Springs sections), TOC wt% was only marginally higher (≤ 0.11%; see Supplemental Data Tables). An additional concern is that carbonate systems are Fe-limited so there must be a source for the reactive Fe (II) (e.g., Berner, 1984; Lyons and Gill, 2009; Raiswell et al., 2018). This leaves the overlying water column as the most likely source of Fe^{2+}; dissolved Fe is typically low in seawater, but the highest concentrations are associated with oxygen minimum zones or at a chemocline (e.g., Rue et al., 1997 and references therein; Severmann et al., 2008). Therefore, the expansion of an oxygen minimum zone (OMZ) onto this shelf area (Fig. 9) was the most plausible source of the Fe^{2+} required for the copious amounts of pyrite formed here during the Ludfordian. Overall, these variations in I/Ca, $\delta^{34}S$, and TOC contents between our study sections on the Western Tennessee Shelf indicate notable regional-scale redox heterogeneities that closely correspond to the changes in facies and faunal reorganizations (see Section 5.1) during the globally documented LKE and associated Lau CIE interval.

5.4. Global implications for late Silurian marine redox conditions and the LKE

As early as the Middle Ordovician, cool, oxygen-deficient, deep waters were moving into the Laurentian epeiric seaway from the continental margin via the Reelfoot Rift Embayment (Kolata et al., 2001). Due to the paleogeographic location and relatively narrow connection to the open ocean during the Silurian, more redox-stratified conditions would have been favored to develop within the Reelfoot Rift Embayment. Consequently, prior to the LKE interval, when sea level was higher (see Sections 4.1.2 and 5.2), an OMZ was likely present adjacent to the deepest parts of the carbonate shelf due to the proximity to the deeper, oxygen-deficient waters within the Reelfoot Rift Embayment (Fig. 9A). The majority of the shelf would have been well-oxygenated, though with some, possibly scattered, areas of reducing (sulfidic) sediment pore-waters (Fig. 9A, D). As eustatic sea level decreased, locally indicated by the shift in microfacies and lithology moving from the Beech River to the Bob members, some amount of restriction could have affected the Western Tennessee Shelf. Limited circulation and mixing with the open ocean would have allowed for marine water columns to become stratified, and thus the OMZ would have expanded higher onto the shelf. As this expansion occured, oxygen-poor waters spread onto the Western Tennessee Shelf and resulted in the nadir in the I/Ca ratios (Fig. 9B, E). The OMZ may have only been weakly established on the middle–upper parts of this shelf as the I/Ca values never reach a minimum of zero (Figs. 4C and 5C) to indicate a complete lack of oxygen, and there is a somewhat subdued local expression of the Lau/Kozlowskii extinction event in this area (i.e. faunal reorganization rather than ecosystem collapse; cf. Barrick et al., 2010). The significant deposition of finely disseminated pyrite that is observed throughout the Brownsport Formation, however, does suggest that there was sulfide present within sediment porewaters, at the sediment-water interface, and possibly in the water column (Gomes and Hurtgen, 2015). Furthermore, an expansion of reducing bottom waters into the area during the LKE and Lau CIE brought Fe^{2+} into this Fe-limited, mixed carbonate and siliciclastic environment leading to the enhancement of pyrite deposition in an otherwise Fe^{2+}-limited shelf area.

Relatively low-oxygen conditions appear to have persisted during initial transgressive conditions following the pronounced lowstand. As sea level rose in the post-CIE recovery interval, possibly to even higher levels than prior to the CIE (Eriksson and Calner, 2008; Johnson, 2010), more connectivity with the Rheic Ocean was likely established and vigorous circulation that led to a contraction of the local OMZ (Fig. 9C, F). While it may be possible that this sea-level driven 're-oxygenation event' oxidized the I^- that was present in the water column, the oxidation of I^- is a slow process (Hardisty et al., 2020). Thus, it is more likely that the reinvigoration of the waters along the shelf with well-oxygenated surface waters from the Rheic Ocean brought in a large pool of IO_3^- during the post-CIE transgression—causing the peak in I/Ca ratios. The high I/Ca values presented here, particularly for the Ladybug and Olive Hill sections, are anomalous for the Paleozoic and represent higher mean and maximum values than those recently reported in a compilation of available Phanerozoic I/Ca datasets (Lu et al., 2018). This may be due to paleoceanographic differences (e.g. water depth, circulation, basin connectivity, etc.) of previously generated I/Ca data sets in comparison to these relatively shallow-water depositional settings (e.g. the Ladybug section).These high values could also be due to preservational and diagenetic differences between our study localities relative to those previously reported. Additionally, the extent of sulfidic sediment porewaters seems to reduce dramatically (based upon the $\delta^{34}S_{pyr}$ records) during this time. In the stratigraphic intervals of higher sea level, before and after the peak values of the Lau CIE, there was also particularly notable diversity in the microfaunal assemblages (i.e., Fig. 4D) and in some cases, this is apparent in the macrofauna (Fig. 2E and 5). The changes in faunal assemblages is most likely connected to the increased oxygenation of this marine environment as evidenced by the I/Ca data as well as higher sea level allowing for more normal marine fauna to return to this shelf area. Similar regional-scale redox heterogeneities are also seen in the Great Basin region along the western Laurentian margin during the Early Ordovician Stairsian extinction event and CIE (Edwards et al., 2018).

The most parsimonious explaination for both the changes in microfacies and local redox conditions is through regional paleoceanography and sea-level changes. It is likely that the changes in sea level seen in the Western Tennessee Shelf are eustatic in nature rather than due to just local or regional scale processes. Observed facies shifts in the carbonate sequences of Gotland and elsewhere hold evidence of similar changes in sea level, with a sea-level lowstand associated with the LKE/CIE interval and higher sea level before and after (Eriksson and Calner, 2008). The same can also be observed in the deeper-water, mixed siliciclastics and carbonates of peri-Gondwana (Lehnert et al., 2007; Manda et al., 2012). These records also align well with global reconstructions of sea level in the late Silurian (e.g., Haq and Schutter, 2008).

All of the spatiotemporal changes to the local redox landscape of the Western Tennessee Shelf were superimposed on global-scale marine redox dynamics during the LKE and Lau CIE interval. Though they were deposited in a basin on another paleocontinent, the trends in the carbon and sulfur isotope data are remarkably similar to those seen in Gotland (Baltica; Bowman et al., 2019), albeit with local variations in magnitude due to depositional setting. The Lau CIE is conspicuously expressed in $\delta^{13}C_{carb}$ in each of the sections studied herein as positive excursions with magnitudes of +4.5 to +6‰ (Figs. 3A, 4A, 5A and 6A) and parallel positive sulfur isotope excursions with magnitudes of +7 to +8‰ in $\delta^{34}S_{CAS}$ are present in the Ladybug and Bath Springs data (Figs. 4B and 6B). The magnitudes of the CIE recorded in this area overlap with studied sections in other basins/paleocontinents, but the magnitude of the positive $\delta^{34}S_{CAS}$ excursion is rather subdued compared to the +30‰ shift documented from Gotland, Sweden (Bowman et al., 2019). This smaller magnitude shift in $\delta^{34}S_{CAS}$ records from TN could be due to varying degrees of pyrite contamination in the extracted CAS (see Section 5.2 above) that could have dampened primary $\delta^{34}S_{CAS}$ values as isotopically-light sedimentary pyrite is pervasive throughout the Brownsport Formation. This could also be due to spatial heterogeneity in the $\delta^{34}S_{SO4}$ values of the late Silurian oceans, implying that sulfate concentrations during this time were relatively low (e.g., Gill et al., 2011b). Additionally, the $\delta^{34}S_{CAS}$ magnitude offsets could be attributed to differences between local depositional environments and

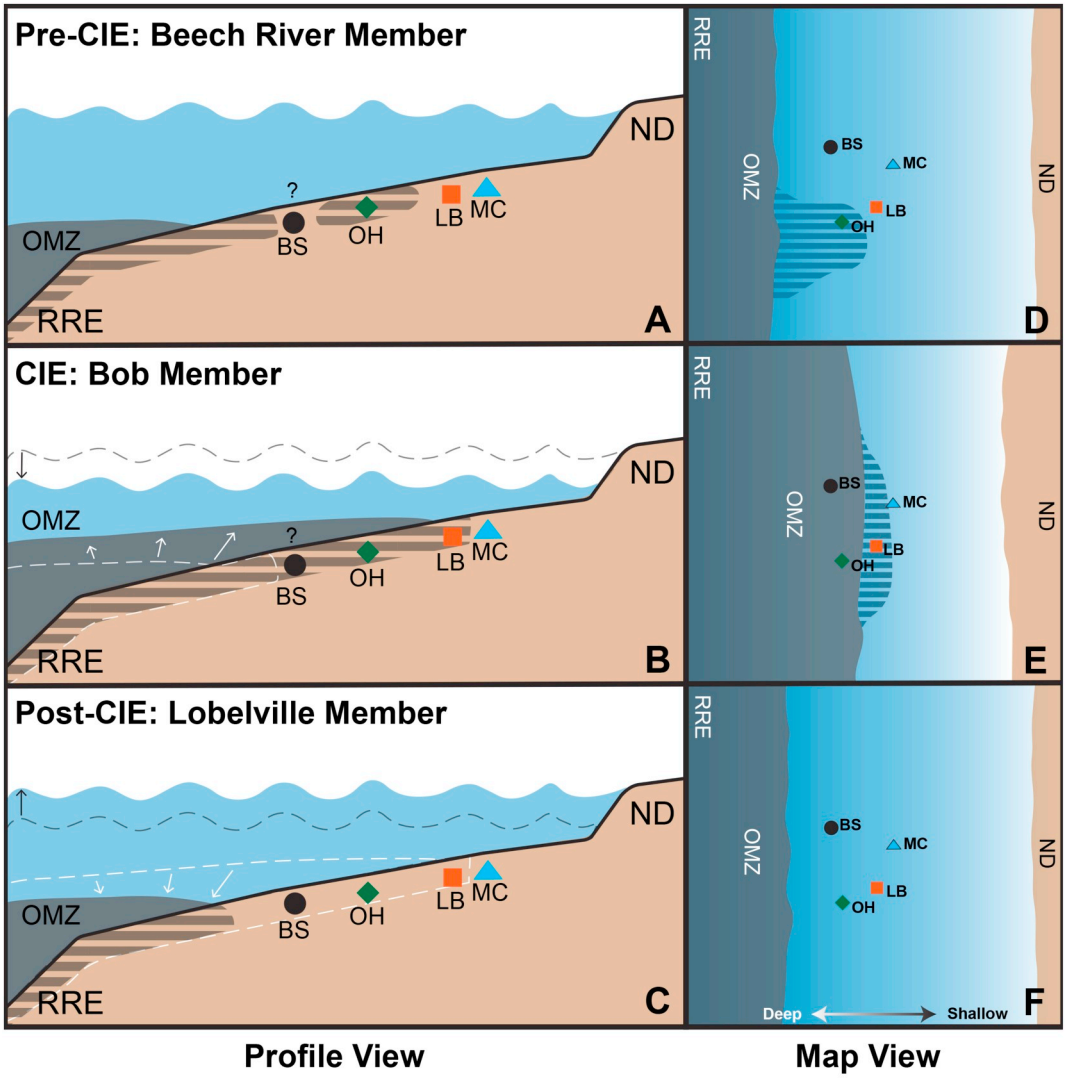

Fig. 9. Schematic reconstruction of the redox and sea-level changes across the Western Tennessee Shelf (see Sections 5.3 and 5.4 for discussion). Relative positions of study sections and pertinent paleogeographic features are noted. A) Pre-carbon isotope excursion (CIE) paleoceanographic reconstruction showing a relatively small area of water column anoxic/euxinic conditions (OMZ) on the deeper part of the carbonate shelf with reducing sediment pore waters evident in at least part of the shelf. B) Reconstruction of paleoceanographic conditions during the peak of the CIE showing an expansion of reducing conditions (anoxic/euxinic) further onto the shelf as sea level falls. C) Post-CIE paleoceanographic reconstruction showing again a relatively small area of water column anoxic/euxinic conditions. Changes in the chemocline and sea level are portrayed in panels B and C using dashed white and black lines, respectively. D–F) Map view of bottom-water redox conditions for each of the time-slices to show the plausible location of oxygen minimum zone (grey) and anoxia/presence of sulfide in porewaters (stripes) on the shelf relative to the study sites. ND: Nashville Dome. RRE: Reelfoot Rift Embayment. MC: Morrison Creek. LB: Ladybug. OH: Olive Hill. BS: Bath Springs. OMZ: oxygen minimum zone. Question mark: reflects minor uncertainty in portions of the I/Ca dataset at BS.

sulfur cycling within these areas, as offsets in $\delta^{34}S_{CAS}$ values have been documented previously in this region during the early Silurian Ireviken CIE (Young et al., 2019). While there are notable offsets in magnitudes and baseline values that are likely related to a combination of the factors and processes described above, all records show the same general trends suggesting increased global pyrite burial rates that would have decreased marine sulfate concentrations.

The paired positive carbon and sulfur isotope excursions support the idea that there was a transitory increase in the amount of organic carbon and pyrite buried in the global oceans throughout the middle Ludfordian, and this was likely due to an expansion of anoxic and/or euxinic seafloor conditions (e.g., Gill et al., 2011a; Owens et al., 2013; Sim et al., 2015; Young et al., 2019). In the mixed carbonate and siliciclastic successions of the Western Tennessee Shelf the falling limb of the $\delta^{34}S_{CAS}$ excursion is recorded for the first time, as it was not documented in the rock record from Gotland, Sweden (Bowman et al., 2019). A slight lag between the peak values of the carbon and sulfur isotope excursion records is expressed in both the Ladybug and Bath Springs sections, which is consistent with the paired C–S isotope records from the Baltic Basin (Bowman et al., 2019). This suggests a slight decoupling of the global C-S cycles during the recovery interval of the Lau CIE, as carbon burial declined prior to pyrite burial and the contraction of euxinia. This could have been the result of continued microbial sulfate reduction fueled by an excess of organic carbon available at or near the sediment/water interface post-carbon burial event. This could also have been due to differences in residence time between carbon and sulfur in the ocean (e.g., Owens et al., 2013). Thus, this detailed regional study provides further evidence of changes in marine redox conditions across the LKE and Lau CIE that are largely consistent with global redox proxies (Bowman et al., 2019) but also highlight local redox heterogeneities and overprints, which are likely present during other Phanerozoic CIE intervals.

6. Conclusions

The stratigraphic trends in the geochemical and carbonate microfacies data reported herein from the four sections along the Western Tennessee Shelf document notable local- to regional-scale redox heterogeneities and faunal reorganizations during the interval of time corresponding to the globally documented Lau/Kozlowskii extinction event and associated Lau CIE. Positive excursions in $\delta^{13}C_{org}$ and $\delta^{34}S_{pyr}$ are largely reflective of changes to the global dissolved inorganic carbon and sulfate pools, respectively. Antithetically correlated trends in I/Ca ratios with $\delta^{13}C$ data in multiple sections indicate a regional incursion of oxygen-poor waters, likely through the expansion of an OMZ upwards along the carbonate shelf. Trends in I/Ca and faunal assemblages are also closely tied to changes in sea level and local marine redox conditions. The large abundance of finely disseminated pyrite, nodular pyrite horizons, high magnitude excursions in $\delta^{34}S_{pyr}$, and isotopic evidence of closed system MSR suggest that at least sediment porewaters, if not parts of the water column along the shelf, were sulfidic/euxinic. Based on both field studies and microfacies analyses, we confirm that the Lau/Kozlowskii extinction event is manifested in the Western Tennessee Shelf area through significant marine faunal reorganizations in the mid-Ludfordian. The global proxy records, $\delta^{13}C_{carb}$ and $\delta^{34}S_{CAS}$, show parallel positive excursions supporting previous hypotheses that rates of organic carbon and pyrite burial increased globally at this time via the expansion of reducing marine bottom-water conditions.

The combination of high-resolution global and local redox proxy records, extensive field-based observations, and detailed microfacies analyses allows for a holistic view of the environmental change(s) that took place in southern Laurentia throughout the LKE and associated Lau CIE interval. On the Western Tennessee Shelf, the sequence of events which we have proposed to explain the spatiotemporal changes to the local redox landscape corresponds well to previous reconstructions of global changes in redox and sea level. This work demonstrates the utility of examining and analyzing more than one locality in a given region when attempting to reconstruct local redox conditions and making inferences about global-scale changes in the ancient oceans, as a variety of factors can influence the preserved signals of local redox in the sedimentary record.

Acknowledgments

Two anonymous reviewers are thanked for their insightful comments that helped to improve this paper, as well as Tom Algeo for his comments and editorial direction. We thank Andrew Kleinberg, Theodore Them II, and Jane Wadhams for assistance with sample collection and geochemical analyses. We would also like to thank Jim Barrick for generously sharing his knowledge of the lithostratigraphy, conodont biostratigraphy, and carbon-isotope chemostratigraphy of the Brownsport Formation in western Tennessee. This research was funded by the National Science Foundation (EAR-1748635 to SAY and JDO). AL acknowledges funding from the Birgit and Hellmuth Hertz' Foundation and the Royal Physiographic Society in Lund. This research was performed at the National High Magnetic Field Laboratory, which is supported by NSF Cooperative Agreement No. DMR-1644770 and the State of Florida.

Conflict of interest: none.

Appendix A. Supplementary data

Supplementary data to this article can be found online at https://doi.org/10.1016/j.palaeo.2020.109799.

References

Amsden, T.W., 1949. Stratigraphy and paleontology of the Brownsport Formation (Silurian) of western Tennessee. Yale Univ. Press Bull. 5 138 p.

Arthur, M.A., Dean, W.E., Pratt, L.M., 1988. Geochemical and climatic effects of increased marine organic carbon burial at the Cenomanian/Turonian boundary. Nature 335, 714–717.

Banner, J.L., Hanson, G.N., 1990. Calculation of simultaneous isotopic and trace element variations during water-rock interaction with applications to carbonate diagenesis. Geochim. Cosmochim. Acta 54, 3123–3137. https://doi.org/10.1016/0016-7037(90)90128-8.

Barrick, J.E., Kleffner, M.A., Gibson, M.A., Peavey, F.N., Karlsson, H.R., 2010. The mid-Ludfordian Lau event and carbon isotope excursion (Ludlow, Silurian) in southern Laurentia – preliminary results. Bull. Geol. Soc. Italy 49, 13–33.

Bathurst, R.G.C., 1987. Diagenetically enhanced bedding in argillaceous platform limestones: stratified cementation and selective compaction. Sedimentology 34, 749–778.

Berner, R.A., 1984. Sedimentary pyrite formation: an update. Geochim. Cosmochim. Acta 48, 605–615.

Berner, R.A., 1994. GEOCARBII: a revised model of atmospheric CO_2 over Phanerozoic Time. Am. J. Sci. 294, 56–91.

Bickert, T., Patzold, J., Samtleben, C., Munnecke, A., 1997. Paleoenvironmental changes in the Silurian indicated by stable isotopes in brachiopod shells from Gotland, Sweden. Geochim. Cosmochim. Acta 61, 2717–2730.

Bond, D.P.G., Grasby, S.E., 2017. On the causes of mass extinctions. Palaeogeogr. Palaeoclimatol. Palaeoecol. 478, 3–29. https://doi.org/10.1016/j.palaeo.2016.11.005.

Bottrell, S.H., Newton, R.J., 2006. Reconstruction of changes in global sulfur cycling from marine sulfate isotopes. Earth-Sci. Rev. 75, 59–83. https://doi.org/10.1016/j.earscirev.2005.10.004.

Bowman, C.N., Young, S.A., Kaljo, D., Eriksson, M.E., Them II, T.R., Hints, O., Martma, M., Owens, J.D., 2019. Linking the progressive expansion of reducing conditions to a stepwise mass extinction event in the late Silurian oceans. Geology 47 (10), 968–972. https://doi.org/10.1130/G46571.1.

Braille, L.W., Hinze, W.J., Sexton, J.L., Keller, G.R., Lidiak, E.G., 1984. Tectonic development of the New Madrid seismic zone. U.S. Geol. Surv. Open File Rep. 84-770, 204–233.

Broadhead, T.W., Gibson, M.A., 1996. Late Silurian sedimentary environments and biotas of west-Central Tennessee. In: Broadhead, T.W. (Ed.), Sedimentary Environments of Silurian Taconia. Univ. Tenn. Dept. Geol. Sci. Stud. Geol., vol. 26. pp. 1–30.

Brüchert, V., Pratt, L.M., 1996. Contemporaneous early diagenetic formation of organic and inorganic sulfur in estuarine sediments from St. Andrew Bay, Florida, USA. Geochim. Cosmochim. Acta 60, 2325–2332.

Calner, M., 2005. A Late Silurian extinction event and anachronistic period. Geology 33 (4), 305–308. https://doi.org/10.1130/G21185.1.

Calner, M., 2008. Silurian global events — at the tipping point of climate change. In: Elewa, A.M.T. (Ed.), Mass Extinctions. Springer-Verlag, Berlin Heidelberg, pp. 21–58.

Canfield, D.E., Thamdrup, B., 1994. The production of S-34-depleted sulfide during bacterial disproportionation of elemental sulfur. Science 266, 1973–1975.

Canfield, D.E., Raiswell, R., Westrich, J.T., Reaves, C.M., Berner, R.A., 1986. The use of chromium reduction in the analysis of reduced inorganic sulfur in sediments and shales. Chem. Geol. 54, 149–155.

Canfield, D.E., Raiswell, R., Bottrell, S., 1992. The reactivity of sedimentary iron minerals toward sulfide. Am. J. Sci. 292, 659–683.

Cherns, L., 1983. The Hemse-Eke boundary: facies relationships in the Ludlow of Gotland. C800. Svergies geologiska undersokning, Sweden, pp. 1–45.

Cocks, L.R.M., Scotese, C.R., 1991. The global paleography of the Silurian Period. Palaeontol. Assoc. Spec. Pap. Paleontol. 44, 109–122.

Cocks, L.R.M., Torsvik, T.H., 2002. Earth geography from 500 to 400 million years ago: a faunal and paleomagnetic review. J. Geol. Soc. Lond. 159, 631–644.

Cramer, B.D., Saltzman, M.R., 2005. Sequestration of 12C in the deep ocean during the early Wenlock (Silurian) positive carbon isotope excursion. Palaeogeogr. Palaeoclimatol. Palaeoecol. 219, 333–349. https://doi.org/10.1016/j.palaeo.2005.01.009.

Cramer, B.D., Saltzman, M.R., 2007. Fluctuations in epeiric sea carbonate production during Silurian positive carbon isotope excursions: A review of proposed paleoceanographic models. Palaeogeogr. Palaeoclimatol. Palaeoecol. 245, 37–45. https://doi.org/10.1016/j.palaeo.2006.02.027.

Dickson, A.J., Jenkyns, H.C., Porcelli, D., van den Boorn, S., Idiz, E., Owens, J.D., 2016. Corrigendum to "Basin-scale controls on the molybdenum-isotope composition of seawater during Ocean Anoxic Event 2 (Late Cretaceous)". Geochim. Cosmochim. Acta 189, 404–405. https://doi.org/10.1016/j.gca.2016.06.025.

Dunham, R.J., 1962. Classification of carbonate Rocks according to depositional texture. In: Ham, W.E. (Ed.), Classification of Carbonate Rocks. Am. Assoc. of Pet. Geol. Mem., pp. 108–121.

Edwards, C.T., Fike, D.A., Saltzman, M.R., Lu, W., Lu, Z., 2018. Evidence for local and global redox conditions at an Early Ordovician (Tremadocian) mass extinction. Earth Planet. Sci. Lett. 481, 125–135. https://doi.org/10.1016/j.epsl.2017.10.002.

Epstein, A.G., Epstein, J.B., Harris, L.D., 1977. Conodont color alteration – an index to organic metamorphism. US Geol. Surv. Prof. Pap. 995, 1–27.

Eriksson, M.E., Calner, M. (Eds.), 2005. The dynamic Silurian Earth: subcommission on Silurian stratigraphy field meeting 2005. Sver. Geol. Unders. Rapporter Meddelanden 121, 1–99.

Eriksson, M.J., Calner, M., 2008. A sequence stratigraphical model for the Late Ludfordian (Silurian) of Gotland, Sweden: implications for timing between changes in sea level, palaeoecology, and the global carbon cycle. Facies 54, 253–276. https://doi.org/10.1007/s10347-007-0128-y.

Eriksson, M.E., Nilsson, E.K., Jeppsson, L., 2009. Vertebrate extinctions and reorganizations during the late Silurian Lau Event. Geology 37 (8), 739–742. https://doi.org/10.1130/G25709A.1.

Flügel, E., 2010. Microfacies of Carbonate Rocks: Analysis, Interpretation and Application. Springer Verlag, Berlin 984 pp.
Gill, B.C., Lyons, T.W., Frank, T.D., 2008. Behavior of carbonate-associated sulfate during meteoric diagenesis and implications for the sulfur isotope paleoproxy. Geochim. Cosmochim. Acta 72, 4699–4711. https://doi.org/10.1016/j.gca.2008.07.001.
Gill, B.C., Lyons, T.W., Jenkyns, H.C., 2011a. A global perturbation to the sulfur cycle during the Toarcian Oceanic Anoxic Event. Earth Planet. Sci. Lett. 312, 484–496. https://doi.org/10.1016/j.epsl.2011.10.030.
Gill, B.C., Lyons, T.W., Young, S.A., Kump, L.R., Knoll, A.H., Saltzman, M.R., 2011b. Geochemical evidence for widespread euxinia in the Later Cambrian Ocean. Nature 469, 80–83. https://doi.org/10.1038/nature09700.
Gomes, M.L., Hurtgen, M.T., 2013. Sulfur isotope systematics of a euxinic, low-sulfate lake: evaluating the importance of the reservoir effect in modern and ancient oceans. Geology 41 (6), 663–666. https://doi.org/10.1130/G34187.1.
Gomes, M.L., Hurtgen, M.T., 2015. Sulfur isotope fractionation in modern euxinic systems: implications for paleoenvironmental reconstructions of paired sulfate-sulfide isotope records. Geochim. Cosmochim. Acta 157, 39–55. https://doi.org/10.1016/j.gca.2015.02.031.
Haq, B.U., Schutter, S.R., 2008. A chronology of Paleozoic Sea-level changes. Science 322, 64–68. https://doi.org/10.1126/science.1161648.
Hardisty, D.S., Lu, Z., Planavsky, N.J., Bekker, A., Philippot, P., Zhou, X., Lyons, T.W., 2014. An iodine record of Paleoproterozoic surface ocean oxygenation. Geology 42 (7), 619–622. https://doi.org/10.1130/G35439.1.
Hardisty, D.S., Lu, Z., Bekker, A., Diamond, C.W., Gill, B.C., Jiang, G., Kah, L.C., Knoll, A.H., Loyd, S.J., Osburn, M.R., Planavsky, N.J., Wang, C., Zhou, X., Lyons, T.W., 2017. Perspectives on Proterozoic surface ocean redox from iodine contents in ancient and recent carbonate. Earth Planet. Sci. Lett. 463, 159–170. https://doi.org/10.1016/j.epsl.2017.01.032.
Hardisty, D.S., Horner, T.J., Wankel, S.D., Blusztajn, J., Nielsen, S.G., 2020. Experimental observations of marine iodide oxidation using a novel sparge-interface MC-ICP-MS technique. Chem. Geol. 532, 119360. https://doi.org/10.1016/j.chemgeo.2019.119360.
Jaanusson, V., 1972. Constituent analysis of an Ordovician limestone from Sweden. Lethaia 5, 217–237.
Jeppsson, L., 1990. An oceanic model for lithological and faunal changes tested on the Silurian record. J. Geol. Soc. Lond. 147, 663–674.
Jeppsson, L., 2005. Conodont-based revisions of the Late Ludfordian on Gotland, Sweden. GFF 127, 273–282.
Jeppsson, L., Talent, J.A., Mawson, R., Simpson, A.J., Andrew, A.S., Calner, M., Whitford, D.J., Trotter, J.A., Sandström, O., Caldon, H.-J., 2007. High-resolution Late Silurian correlations between Gotland, Sweden and the Broken River region, NE Australia: lithologies, conodonts and isotopes. Palaeogeogr. Palaeoclimatol. Palaeoecol. 245, 115–117.
Johnson, M.E., 2010. Tracking Silurian eustasy: Alignment of empirical evidence or pursuit of deductive reasoning? Palaeogeogr. Palaeoclimatol. Palaeoecol. 296, 276–284. https://doi.org/10.1016/j.palaeo.2009.11.024.
Jones, D.S., Fike, D.A., 2013. Dynamic sulfur and carbon cycling through the end-Ordovician extinction revealed by paired sulfate-pyrite $\delta^{34}S$. Earth Planet. Sci. Lett. 363, 144–155. https://doi.org/10.1016/j.epsl.2012.12.015.
Kaljo, D., Kiipli, T., Martma, T., 1997. Carbon isotope event markers through the Wenlock–Pridoli sequence in Ohesaare (Estonia) and Priekule (Latvia). Palaeogeogr. Palaeoclimatol. Palaeoecol. 132, 211–224.
Kampschulte, A., Bruckschen, P., Strauss, H., 2001. The sulphur isotopic composition of trace sulphates in Carboniferous brachiopods: implications for coeval seawater, correlation with other geochemical cycles and isotope stratigraphy. Chem. Geol. 175 (1–2), 149–173.
Kolata, D.R., Huff, W.D., Bergström, S.M., 2001. The Ordovician Sebree Trough: an oceanographic passage to the Midcontinent United States. Bull. Geol. Soc. Am. 113 (8), 1067–1078.
Koren, T.N., 1993. Main event levels in the evolution of the Ludlow graptolites. Geol. Correl. 1, 44–52.
Kump, L.R., Arthur, M.A., 1999. Interpreting carbon-isotope excursions: carbonates and organic matter. Chem. Geol. 161, 181–198.
Kump, L.R., Arthur, M.A., Patzkowsky, M.E., Gibbs, M.T., Pinkus, D.S., Sheehan, P.M., 1999. A weathering hypothesis for glaciation at high atmospheric pCO_2 during the Late Ordovician. Palaeogeogr. Palaeoclimatol. Palaeoecol. 152, 173–187.
Lau, K.V., Maher, K., Altiner, D., Kelley, B.M., Kump, L.R., Lehrmann, D.J., Silva-Tamayo, J.C., Weaver, K.L., Yu, M., Payne, J., 2016. Marine anoxia and delayed Earth system recovery after the end-Permian extinction. Proc. Natl. Acad. Sci. 113 (9), 2360–2365. https://doi.org/10.1073/pnas.1515080113.
Leavitt, W.D., Halevy, I., Bradley, A.S., Johnston, D.T., 2013. Influence of sulfate reduction rates on the Phanerozoic sulfur isotope record. Proc. Natl. Acad. Sci. 110, 11244–11249. https://doi.org/10.1073/pnas.1218874110.
Lehnert, O., Fryda, J., Buggisch, W., Munnecke, A., Nützel, A., Križ, J., Manda, S., 2007. $\delta^{13}C$ records across the late Silurian Lau event: new data from middle palaeo-latitudes of northern peri-Gondwana (Prague Basin, Czech Republic). Palaeogeogr. Palaeoclimatol. Palaeoecol. 245, 227–244. https://doi.org/10.1016/j.palaeo.2006.02.022.
Lindskog, A., Eriksson, M.E., 2017. Megascopic processes reflected in the microscopic realm: sedimentary and biotic dynamics of the Middle Ordovician “orthoceratite limestone” at Kinnekulle, Sweden. GFF 139, 163–183. https://doi.org/10.1080/11035897.2017.1291538.
Lindström, M., 1984. Ordovician red limestone blackened by modern diffusion of H2S. GFF 106, 40.
Lu, Z., Jenkyns, H.C., Rickaby, R.E.M., 2010. Iodine to calcium ratios in marine carbonate as a paleoredoxproxy during oceanic anoxic events. Geology 38 (12), 1107–1110. https://doi.org/10.1130/G31145.1.
Lu, Z., Hoogakker, B.A.A., Hillenbrand, C.-D., Zhou, X., Thomas, E., Gutchess, K.M., Lu, W., Jones, L., Rickaby, R.E.M., 2016. Oxygen depletion recorded in upper waters of the glacial Southern Ocean. Nat. Commun. 7, 1–8. https://doi.org/10.1038/ncomms11146.
Lu, W., Wörndle, S., Halverson, G.P., Zhou, X., Bekker, A., Rainbird, R.H., Hardisty, D.S., Lyons, T.W., Lu, Z., 2017. Iodine proxy evidence for increased ocean oxygenation during the Bitter Springs Anomaly. Geochem. Perspect. Lett. 5, 53–57. https://doi.org/10.7185/geochemlet.1746.
Lu, W., Ridgwell, A., Thomas, E., Hardisty, D.S., Luo, G., Algeo, T.J., Saltzman, M.R., Gill, B.C., Shen, Y., Ling, H., Edwards, C.T., Whalen, M.T., Zhou, X., Gutchess, K.M., Jin, L., Rickaby, R.E.M., Jenkyns, H.C., Lyons, T.W., Lenton, T.M., Kump, L.R., Lu, Z., 2018. Late inception of a resiliently oxygenated upper ocean. Science 361, 174–177. https://doi.org/10.1126/science.aar5372.
Lu, W., Dickson, A.J., Thomas, E., Rickaby, R.E.M., Chapman, P., Lu, Z., 2019. Refining the planktic foraminiferal I/Ca proxy: results from the Southeast Atlantic Ocean. Geochim. Cosmochim. Acta. https://doi.org/10.1016/j.gca.2019.10.025.
Lyons, T.W., Gill, B.C., 2009. The worm turned, and the ocean followed. Proc. Natl. Acad. Sci. 106 (20), 8081–8082. https://doi.org/10.1073/pnas.0903380106.
Lyons, T.W., Walter, L.M., Gellatly, A.M., Martini, A.M., Blake, R.E., 2004. Sites of anomalous organic remineralization in the carbonate sediments of South Florida, USA: the sulfur cycle and carbonate-associated sulfate. In: Amend, J.P., Edwards, K.J., Lyons, T.W. (Eds.), Sulfur Biogeochemistry—Past and Present. Geol. Soc. Am. Spec. Pap., vol. 379. pp. 161–176.
Manda, S., Štorch, P., Slavík, L., Fryda, J., Križ, J., Tasáryová, A., 2012. The graptolite, conodont and sedimentary record through the late Ludlow Kozlowskii Event (Silurian) in the shale-dominated succession of Bohemia. Geol. Mag. 149 (3), 507–531. https://doi.org/10.1017/S0016756811000847.
Marenco, P.J., Corsetti, F.A., Hammond, D.E., Kaufman, A.J., Bottjer, D.J., 2008. Oxidation of pyrite during extraction of carbonate associated sulfate. Chem. Geol. 247 (1–2), 124–132. https://doi.org/10.1016/j.chemgeo.2007.10.006.
Martma, T., Brazauskas, A., Kaljo, D., Kaminskas, D., Musteikis, P., 2005. The Wenlock-Ludlow carbon isotope trend in the Vidukle core, Lithuania, and its relations with oceanic events. Geol. Q. 49 (2), 223–234.
McAdams, N.E.B., Cramer, B.D., Bancroft, A.M., Melchin, M.J., Devera, J.A., Day, J.E., 2019. Integrated $\delta^{13}C_{carb}$, conodont, and graptolite biogeochemistry of the Silurian from the Illinois Basin and stratigraphic revision of the Bainbridge Group. Geol. Soc. Am. Bull. 113 (1–2), 335–352. https://doi.org/10.1130/B32033.1.
Munnecke, A., Samtleben, C., Bickert, T., 2003. The Ireviken Event in the lower Silurian of Gotland, Sweden – relation to similar Palaeozoic and Proterozoic events. Palaeogeogr. Palaeoclimatol. Palaeoecol. 195, 99–124. https://doi.org/10.1016/S0031-0182(03)00304-3.
Munnecke, A., Calner, M., Harper, D.A.T., Servais, T., 2010. Ordovician and Silurian Sea-water chemistry, sea level, and climate: a synopsis. Palaeogeogr. Palaeoclimatol. Palaeoecol. 296, 389–413. https://doi.org/10.1016/j.palaeo.2010.08.001.
Odin, G.S., 1988. Glaucony from the Gulf of Guinea. Dev. Sedimentol. 45, 225–247.
Olgun, O., 1987. Komponenten-Analyse und Conodonten-Stratigraphie der Orthoceratenkalksteine im Gebiet Falbygden, Västergötland, Mittelschweden. Sveriges Geologiska Undersökning Ca70, pp. 1–78.
Owens, J.D., Gill, B.C., Jenkyns, H.C., Bates, S.M., Severmann, S., Kuypers, M.M.M., Woodfine, R.G., Lyons, T.W., 2013. Sulfur isotopes track the global extent and dynamics of euxinia during Cretaceous Oceanic Anoxic Event 2. Proc. Natl. Acad. Sci. 110 (46), 18407–18412. https://doi.org/10.1073/pnas.1305304110.
Owens, J.D., Lyons, T.W., Hardisty, D.S., Lowery, C.M., Lu, Z., Lee, B., Jenkyns, H.C., 2017. Patterns of local and global redox variability during the Cenomanian-Turonian Boundary Event (Ocean Anoxic Event 2) recorded in carbonates and shales from Central Italy. Sedimentology 64, 168–185. https://doi.org/10.1111/sed.12352.
Owens, J.D., Lyons, T.W., Lowery, C.M., 2018. Quantifying the missing sink for global organic carbon burial during a cretaceous oceanic anoxic event. Earth Planet. Sci. Lett. 499, 83–94. https://doi.org/10.1016/j.epsl.2018.07.021.
Pate, W.F., Bassler, R.S., 1908. The Late Niagaran strata of West Tennessee. U.S. Natl. Mus. Proc. 34 135 p.
Powers, M.C., 1953. A new roundness scale for sedimentary particles. J. Sediment. Petrol. 23, 117–119.
Railsback, L.B., Holland, S.M., Hunter, D.M., Jordan, E.M., Diaz, J.R., Crowe, D.E., 2003. Controls on Geochemical Expression of Subaerial Exposure in Ordovician Limestones from the Nashville Dome, Tennessee, U.S.A. J. Sediment. Res. 73, 790–805. https://doi.org/10.1306/020503730790.
Raiswell, R., Hardisty, D.S., Lyons, T.W., Canfield, D.E., Owens, J.D., Planavsky, N.J., Poulton, S.W., Reinhard, C.T., 2018. The iron paleoredox proxies: a guide to the pitfalls, problems and proper practice. Am. J. Sci. 318, 491–526. https://doi.org/10.2475/05.2018.03.
Reinhard, C.T., Planavsky, N.J., Robbins, L.J., Partin, C.A., Gill, B.C., Lalonde, S.V., Bekker, A., Konhauser, K.O., Lyons, T.W., 2013. Proterozoic Ocean redox and biogeochemical stasis. Proc. Natl. Acad. Sci. 110 (14), 5357–5362. https://doi.org/10.1073/pnas.1208622110.
Ries, J.B., Fike, D.A., Pratt, L.M., Lyons, T.W., Grotzinger, J.P., 2009. Superheavy pyrite ($\delta^{34}S_{pyr} > \delta^{34}S_{CAS}$) in the terminal Proterozoic Nama Group, southern Namibia: a consequence of low seawater sulfate at the dawn of animal life. Geology 37 (8), 743–746. https://doi.org/10.1130/G25775A.1.
Rue, E.L., Smith, G.J., Cutter, G.A., Bruland, K.W., 1997. The response of trace element redox couples to suboxic conditions in the water column. Deep-Sea Res. I Oceanogr. Res. Pap. 44, 113–134.
Saltzman, M.R., 2001. Silurian delta C-13 stratigraphy: a view from North America. Geology 29 (8), 671–674.
Saltzman, M.R., 2002. Carbon isotope ($\delta^{13}C$) stratigraphy across the Silurian-Devonian

transition in North America: evidence for a perturbation of the global carbon cycle. Palaeogeogr. Palaeoclimatol. Palaeoecol. 187, 83–100.
Saltzman, M.R., Thomas, E., 2012. Carbon isotope stratigraphy. In: Goldstein, F.M., Ogg, J.G., Schmitz, M. (Eds.), Geologic Time Scale 2012, pp. 207–267. https://doi.org/10.1016/B978-0-444-59425-9.00011-1.
Severmann, S., Lyons, T.W., Anbar, A., McManus, J., Gordon, G., 2008. Modern iron isotope perspective on the benthic iron shuttle and the redox evolution of ancient oceans. Geology 36 (6), 487–490. https://doi.org/10.1130/G24670A.
Sim, M.S., 2019. Effect of sulfate limitation on sulfur isotope fractionation in batch cultures of sulfate reducing bacteria. Geosci. J. 23 (5), 687–694. https://doi.org/10.1007/s12303-019-0015-x.
Sim, M.S., Ono, S., Hurtgen, M.T., 2015. Sulfur isotope evidence for low and fluctuating sulfate levels in the late Devonian Ocean and the potential link with the mass extinction event. Earth Planet. Sci. Lett. 419, 52–62. https://doi.org/10.1016/j.epsl.2015.03.009.
Spiridonov, A., Stankevič, R., Gečas, T., Šilinskas, T., Brazauskas, A., Meidla, T., Ainsaar, L., Musteikis, Radzevičius S., 2017. Integrated record of Ludlow (Upper Silurian) oceanic geobioevents – coordination of changes in conodont, and brachiopod faunas, and stable isotopes. Gondwana Res. 51, 272–288.
Stricanne, L., Munnecke, A., Pross, J., 2006. Assessing mechanisms of environmental change: Palynological signals across the Late Ludlow (Silurian) positive isotope excursion ($\delta^{13}C$, $\delta^{18}O$) on Gotland, Sweden. Palaeogeogr. Palaeoclimatol. Palaeoecol. 230, 1–31. https://doi.org/10.1016/j.palaeo.2005.07.003.
Swart, P.K., Eberli, G., 2005. The nature of the $\delta^{13}C$ of periplatform sediments: Implications for stratigraphy and the global carbon cycle. Sediment. Geol. 175, 115–129. https://doi.org/10.1016/j.sedgeo.2004.12.029.
Talent, J.A., Mawson, R., Andrew, A.S., Hamilton, P.J., Whitford, D.J., 1993. Middle Paleozoic extinction events: faunal and isotopic data. Palaeogeogr. Palaeoclimatol. Palaeoecol. 104, 139–152.
Torsvik, T.H., Cocks, L.R.M., 2017. Silurian. In: Earth History and Palaeogeography. Cambridge University Press, Cambridge, pp. 124–137. https://doi.org/10.1017/9781316225523.008.
Urbanek, A., 1993. Biotic crises in the history of the upper Silurian graptoloids: a paleobiological model. Hist. Biol. 7, 29–50.
Urbanek, A., Radzevičius, S., Kozłowska, A., Teller, L., 2012. Phyletic evolution and iterative speciation in the persistent Pristiograptus dubius lineage. Acta Palaeontol. Pol. 57 (3), 589–611. https://doi.org/10.4202/app.2010.0070.
Vaquer-Sunyer, R., Duarte, C., 2008. Thresholds of hypoxia for marine biodiversity. Proc. Natl. Acad. Sci. 105, 15452–15457.
Wingforss-Lange, J., 1999. Carbon isotope ^{13}C enrichment in Upper Silurian (Withcliffian) marine calcareous rocks in Scania, Sweden. GFF 121, 273–279.
Wong, G.T.F., Brewer, P.G., 1977. The marine chemistry of iodine in anoxic basins. Geochim. Cosmochim. Acta 41, 151–159.
Wotte, T., Shields-Zhou, G.A., Strauss, H., 2012. Carbonate-associated sulfate: experimental comparisons of common extraction methods and recommendations toward a standard analytical protocol. Chem. Geol. 326-327, 132–144. https://doi.org/10.1016/j.chemgeo.2012.07.020.
Young, S.A., Kleinberg, A., Owens, J.D., 2019. Geochemical evidence for expansion of marine euxinia during an early Silurian (Llandovery–Wenlock boundary) mass extinction. Earth Planet. Sci. Lett. 513, 187–196. https://doi.org/10.1016/j.epsl.2019.02.023.
Zhang, F., Romaniello, S.J., Algeo, T.J., Lau, K.V., Clapham, M.E., Richoz, S., Herrmann, A.D., Smith, H., Horacek, M., Anbar, A.D., 2018. Multiple episodes of extensive marine anoxia linked to global warming and continental weathering following the latest Permian mass extinction. Sci. Adv. 4, e1602921. https://doi.org/10.1126/sciadv.1602921.
Zhou, X., Thomas, E., Rickaby, R.E.M., Winguth, A.M.E., Lu, Z., 2014. I/Ca evidence for upper ocean deoxygenation during the PETM. Paleoceanography 29, 1–12. https://doi.org/10.1002/2014PA002702.
Zhou, X., Jenkyns, H.C., Owens, J.D., Junium, C.K., Zheng, X.-Y., Sageman, B.B., Hardisty, D.S., Lyons, T.W., Ridgewell, A., Lu, Z., 2015. Upper Ocean oxygenation dynamics from I/Ca ratios during the Cenomanian-Turonian OAE 2. Paleoceanography 30, 510–526. https://doi.org/10.1002/2014PA002741.